Energy Storage Materials 51 (2022) 789–805

Contents lists available at ScienceDirect

Energy Storage Materials

journal homepage: www.elsevier.com/locate/ensm

Architectural van der Waals Bi_2S_3/Bi_2Se_3 topological heterostructure as a superior potassium-ion storage material

Yi-Yen Hsieh, Hsing-Yu Tuan *

Department of Chemical Engineering, National Tsing Hua University, Hsinchu 30013, Taiwan

ARTICLE INFO

Keywords:
Van der Waals
Heterostructures
Potassium
Battery
Capacitor

ABSTRACT

We design a hexagram-like 1D/2D van der Waals heterostructure composed of regularly crosslinked aligned 1D Bi_2S_3 nanowires on 2D Bi_2Se_3 nanoplates, termed Bi_2S_3/Bi_2Se_3 vdWHs, for use as anode materials for potassium ion batteries (PIBs) and hybrid capacitors (PIHCs). Thanks to the mixed dimensional topological heterostructures, the abundant network-contacted heterojunctions facilitate ordered ion/electron transport around the surface network and interior topological materials, and simultaneously promoting the K^+ diffusion, electron transfer, and electrolyte infiltration. The Bi_2S_3/Bi_2Se_3 vdWHs deliver an attractive specific capacity over 600 mA h g^{-1} at 50 mA g^{-1}, a high-rate capability up to 2500 mA g^{-1}, and excellent cycling stability. Theoretical models, in tandem with operando X-ray diffraction and HRTEM analysis reveal the behavior of heterogeneous interfacial reaction in terms of the trapping ability and diffusion kinetics, confirming the reversible conversion reaction of Bi_2S_3/Bi_2Se_3 vdWHs. Finally, the full cells of PIBs and PIHCs coupled with Bi_2S_3/Bi_2Se_3 vdWHs anodes exhibit excellent performances of 208 and 106 Wh kg^{-1} over 850 and 3000 cycles, respectively, demonstrating their feasibility towards practical applications. Our study provides a new insight into architectural strategies for heterogeneous interfaces to realize intelligent kinetic control strategies of chalcogenide topological materials for advanced energy storage.

1. Introduction

Lithium-ion energy storages have been widely used in portable and electric vehicle energy storage devices due to their high theoretical energy density and electrochemical stability. However, the limited and uneven lithium sources impose significant limitations on their wider applications [1]. Potassium-ion storages are beneficial for low-cost, high-energy-density full batteries owing to their abundant resources and low standard redox potential. Typically, anode materials in potassium ion batteries (PIBs) can be divided into three mechanism-typed materials, including intercalation, alloying, and conversion [2]. In the pursuit of high-capacity performance, the 2D silicon materials can deliver high capacity, high-rate capability, and durable structure in lithium-ion system [3,4]. Meanwhile, conversion-typed metal sulfides or selenides in potassium-ion system have been regarded as the promising and desirable materials. Conversion-type materials of various shapes, such as two-dimensional materials (e.g., nanosheet [5], nanoplate [6]), one-dimensional materials (e.g., nanowire, [7] nanorod, [8] nanoruler, [9]), zero-dimensional materials (e.g., nanoparticles, [10,11] nanosphere [12]), and self-assembled nanonetwork from nanorods with facet modification [13], have been shown to possess suitable ion diffusion channels, high ionic conductivity, and fast ion mobility. A volume strain-relaxation electrode consist of 0D red phosphorus and 1D carbon nanofibers exhibited high reversible capacities and extraordinary durability, where the usage of carbon materials can further enhance the diffusion kinetics of K^+ due to their good electron/ion conductivity and structural durability [14]. There are also previous literatures constructing the 1D carbon materials with 0D conversion-type materials, such as candied-haws-like FeS_2@C core–shell structures [15] and SnS-confined multichannel carbon nanofibers [16]. Nevertheless, the drawbacks of employing metal chalcogenides still pose various difficulties, including severe volume variation, sluggish kinetic diffusion, and most importantly, the shuttle effect during the cycling process. Currently, heterointerface engineering controlled by dimensionality and composition effectively improve the kinetic behavior and electrochemical performance in metal chalcogenides [17]. However, its electrochemical behavior is still far from applicable due to the unavoidable loss of active material and excessive lattice distortion in the

* Corresponding author.
E-mail address: hytuan@che.nthu.edu.tw (H.-Y. Tuan).

https://doi.org/10.1016/j.ensm.2022.07.020
Received 2 May 2022; Received in revised form 8 July 2022; Accepted 12 July 2022
Available online 16 July 2022

heterostructure during charge/discharge process. Indeed, common interface engineering may not fully overcome the limitations and concerns of conversion-type materials in K^+ storage. Therefore, the optimal orientation relationship of two materials (*e.g.*, growth direction, preferential facet, attached angle) is crucial for constructing heterojunctions to address the diffusion kinetics of K^+ storages.

Covalent heterostructures are driven by unoccupied bonds on the surface of crystalline materials to minimize surface energy, suggesting that even small lattice mismatches can induce crystal distortions and dislocations. Shi et al. adopted the charge density difference and partial density of states to reveal that the existence of strong covalent nature between Ni_2P and N, P-doped carbon nanosheet, which can significantly prolong the cyclability [18]. Heterostructures composed of different dimensional materials must consider their lattice mismatch and heterogeneous boundaries between the junction materials. For example, based on the hexagonal crystal structures of WS_2 and MoS_2, Lai et al. showed high-resolution ADF-STEM images to confirm the connection between two transition metals and the formation of in-plane heterostructures [19]. Shan et al. demonstrated excellent performance with a configuration of small lattice-mismatched semi-coherent phase boundaries of $CoSe_2$ and $FeSe_2$ [20]. Furthermore, if the heterointerface between two materials consists of different crystal systems and dimensions, van der Waals (vdW) epitaxy and assembly become a key route to construct multifunctional materials. The strategy of constructing VS_4/SnS@C vdW heterostructures and the effective entrapment effect to stabilize metal polysulfides can maintain the reversibility of electrochemical reactions [21]. To further solve the above-mentioned challenges, carbon-based heterostructures formed by contacting carbon with metal chalcogenides are usually adopted to reinforce the cycling life of half cells, thereby enhancing the conductivity and

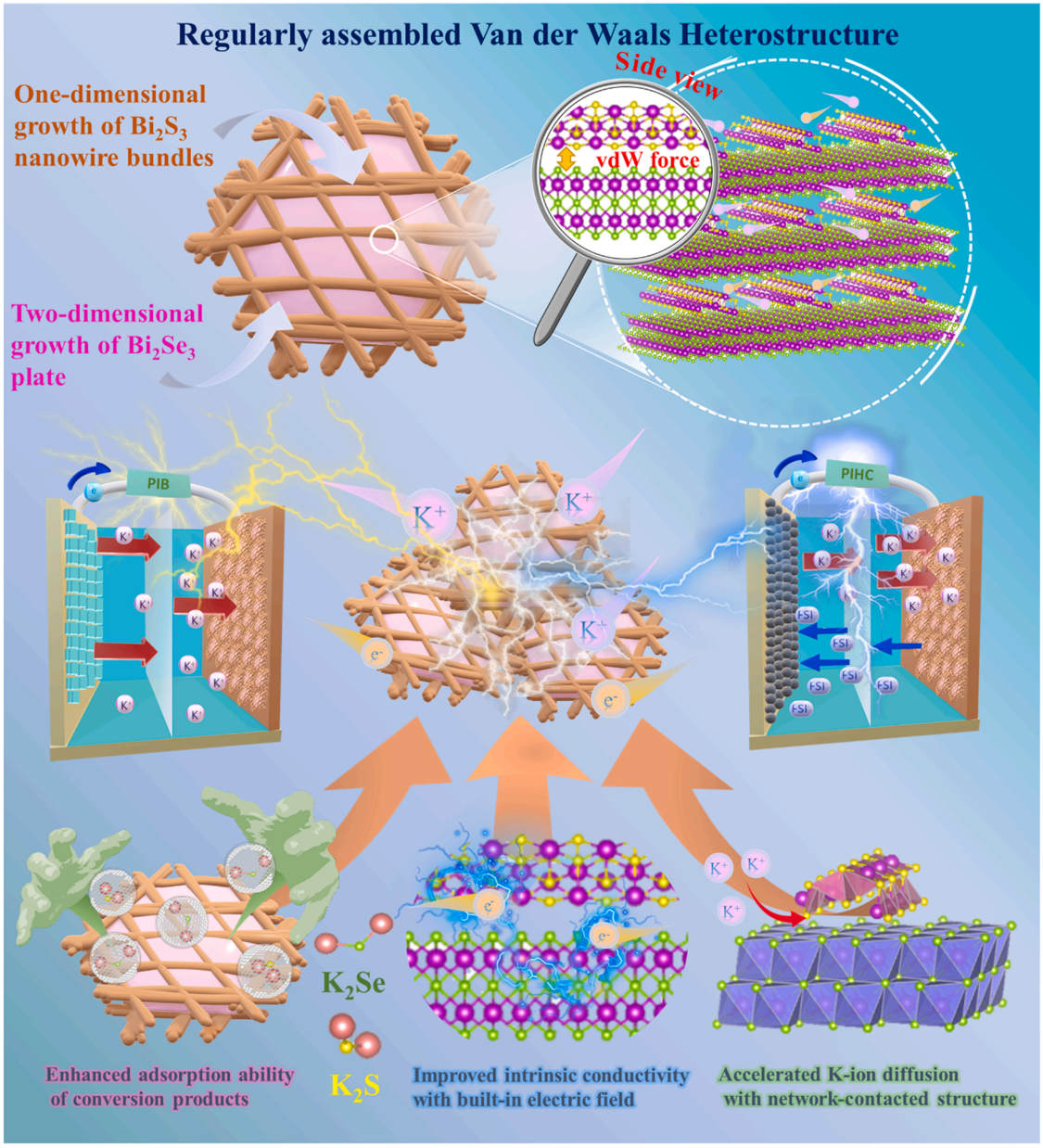

Scheme 1. Schematic illustration of the formation of Bi_2S_3/Bi_2Se_3 vdWHs, and its working mechanism for potassium-ion storage applied on PIB and PIHC full cells. The Bi_2S_3/Bi_2Se_3 vdWHs composed of [001]-orientated growth of Bi_2S_3 nanowire bundles with the lowest surface energy of (010)-exposed plane and [hk0]-orientated growth of Bi_2Se_3 nanoplates enhances the adsorption ability of active intermediates, intrinsic conductivity as well as K^+ kinetic diffusion through p-n junction engineering and rich network-contacted heterointerfaces. The implementation of Bi_2S_3/Bi_2Se_3 vdWHs in full cell configuration of PIBs and PIHCs are demonstrated.

trapping capability of materials. Guo et al. designed the hetero--CoO/Co_3S_4 nanoparticles embedded in N-doped carbon frameworks, exhibiting excellent rate capability and capacity contribution in sodium-ion storages [22]. Wang et al. demonstrated a novel 2D-based vdW heterostructure, $Bi_{0.51}Sb_{0.49}OCl$/rGO, which was not restrained by lattice matching and processing compatibility [23].

However, mixed dimensional heterointerfaces with specific orientations are still difficult to design due to anisotropic crystal growth mechanism and intrinsic lattice mismatch. Meanwhile, the composition of mixed dimensions is difficult to control, leading to interruption of transport paths. Therefore, precise structural refinement and directional interface modulation are required for advanced electrode materials in state-of-the-art PIB storage. Indeed, the internal diffusion of heterointerface are greatly enhanced through the junction modification with electric features of different composition. Inspired by the difference of valence band and energy bandgap, p-n junctions with built-in electric field can induce the directional migration of electrons and holes, facilitating efficient charge transport of heterointerfaces [24]. Based on density functional theory (DFT), changes in electrical properties of heterostructure can reveal junction formation and charge redistribution, improving structural conductivity and stability. In addition to the junction engineering, materials of various dimensions can also provide their different functions and characteristics. The interrelationship between mixed-dimensional materials and their synergetic enhancement, including excellent electron mobility, good mechanical property, large surface area, charge transfer channels, easy electrolyte infiltration, *etc*. [25–27], may bring positive effects on electrochemical performance.

In this study, we design regularly-assembled vdW topological heterostructures that can promote the K^+ diffusion kinetics and electron transportation *via* both lateral and vertical pathways, as illustrated in Scheme 1. The networks formed by Bi_2S_3 nanowires are cross-linked at certain angles and orientations, and stacked with the surface lattice of Bi_2Se_3 nanoplates, so called Bi_2S_3/Bi_2Se_3 vdWHs. The [001]-orientated Bi_2S_3 with (010)-exposed plane assemble directionally along the [hk0]-orientated Bi_2Se_3 with (001)-exposed top surface. Crosslinked wire-contact phase boundaries are evaluated to form network-contact heterointerfaces that unravel rich heterojunctions with the built-in electric field. Electrochemical analysis and DFT calculations show that the novel heterostructures have good mechanical strength and multi-channel electron/ion pathways thanks to the enhanced hetero-interconnection effect. The vdW epitaxy and void space between the heterointerface and nanowire bundles can withstand lattice distortion during cycling, respectively, while providing a migration path of K^+ from the heterointerface to Bi_2Se_3 and increasing adsorption sites for trapping active materials point. Therefore, Bi_2S_3/Bi_2Se_3 vdWHs provide an enhanced electronic conductivity and entrapment effect, and accelerate K^+ diffusion in PIBs and PIHCs.

2. Results and discussion

2.1. Structure characterization

The fabrication process of Bi_2S_3/Bi_2Se_3 vdWHs is shown in Fig. 1a. A facile one-step solvothermal strategy was used to tune kinetic reaction rates and orderly assembled heterostructures in high yields. First, $BiCl_3$ and SeO_2 were dissolved in triethylene glycol containing PVP surfactant and stirred to form a homogeneous solution. Then a sufficient amount of TAA was added to the above solution as a sulfur source, and the color changed from colorless to brown, indicating that the addition of TAA formed a Bi-S nucleus. After stirring for a certain time, the final product was obtained. The kinetics-controlled growth was conducted in the presence of capping agent and viscous solvent to proceed regular assembly of 1D Bi_2S_3 and 2D Bi_2Se_3 (Bi_2S_3/ Bi_2Se_3 vdWHs). The vdW heteroepitaxy can alleviate the lattice distortion of mismatch materials during regularly assembled 1D/2D network/nanoplate to avoid the lattice misfit of two materials due to different crystal systems and lattice parameters [28–30]. The individual chains of PVP polymer interact with each other through the hydrogen bonding and hydrophobic interaction, and then self-assemble into polymer fibers, which can act as a template to control the morphology [31]. Therefore, the PVP chains would selectively adsorbed on (001) and (hk0) facet of Bi_2Se_3 and Bi_2S_3, respectively, to effectively control their morphology and growth direction of nanoplates and nanowire bundles [32]. In addition, the high viscosity of triethylene glycol can limit the surface diffusion rate of Bi-S nucleus on the no-dangling-bond Bi_2Se_3 surface to proceed the nanowires grow regularly epitaxially along the lattice edges of the nanoplates. The above-mentioned parameters could change the kinetic barrier of hydrothermal reaction. If we change these experimental parameters, including long stirring time, fast stirring rate (Fig. S1a), replacing the solvent (Fig. S1b), no addition of PVP (Fig. S1c), and different S/Se molar ratio, the Bi_2S_3 nanowire bundles would not well-crosslink on the Bi_2Se_3 nanoplates [33]. The growth direction of Bi_2Se_3 nanoplates is the [hk0] direction with the (001) exposed facet, while the Bi_2S_3 nanowires grow along the [001] direction with the lower surface energy of the (010) exposed face. The high-magnification field-emission scanning electron microscopy (FESEM) image (Figs. 1b–d and S2) demonstrates the regular growth of Bi_2S_3 with intersection angle of 60^o (red mark in Fig. 1e) of each nanowire bundles along the rhombohedral lattice of Bi_2Se_3. In contrast to Bi_2S_3/ Bi_2Se_3 vdWHs, Bi_2Se_3 nanoplates and Bi_2S_3 nanowires were synthesized using the same method in the supporting information of Figs. S3, S4. Furthermore, we also synthesized the heterostructure at different Se/S precursor ratio. When the molar ratio of SeO_2: TAA was 2:1, the thickness of Bi_2Se_3 nanoplates increased with higher Se concentration in Figs. S5a and S6a, which was around 450 nm, resulting in the edge-to-edge assembly of nanowire bundles and nanoplates. The ultralong Bi_2S_3 nanowires and random-aligned structure were grown at higher concentration of TAA (SeO_2: TAA= 1: 2) in Fig. S6c. It is worth noting that the Bi_2S_3 nanowires were well-crosslinked on the top face of Bi_2Se_3 nanoplates with suitable thickness of ~200 nm (Fig. S5b) only at same molar ratio of SeO_2 and TAA, as shown in Fig. S6b. Therefore, the corresponding scheme of heterostructures with various precursor concentration demonstrated that different S/Se ratio induced different morphology in Fig. S7. The element composition and distribution detected by energy-dispersive X-ray spectroscopy (EDS) corroborate that Se and S are distributed within the centra and crosslinked network of heterostructure, respectively. Meanwhile, the distribution of Bi elements is located throughout the heterostructure. The corresponding mapping results of elemental ratio are given in Fig. S, which is consistent with the stoichiometry ratio of Bi_2Se_3 and Bi_2S_3. To further investigate the formation of the vdWHs, transmission electron microscopy (TEM) images in Figs. 1f and S9 confirm the two-phase feature of the hybrid. The (001)-exposed plane of Bi_2Se_3 nanoplates can be verified by high-resolution TEM (HRTEM) in Fig. 1h and its fast Fourier transformation (FFT) with lattice spacing of ~2.07 Å assigned to the equivalence of (110) and (2–10) plane. The (300) lattice point can also be detected when the band axis of Bi_2Se_3 is in the [001] direction, which we assign as the (001) plane of the Bi_2Se_3 nanoplate according to Bragg's law. The regional axis of the [010] plane in Bi_2S_3 is perpendicular to the predominantly exposed (010) plane, confirmed by the d-spacings of (002), (200) and (101) (Fig. 1i). It is worth mentioning that the preferential growth of nanowires in the [001] direction is due to the fact that the surface energy of the (001) plane is higher than that of the (100) and (010) planes [34,35]. The low surface energy of the (010) plane comes from no-dangling-bond surface [36]. According to the selected-area electron diffraction (SAED) pattern in Fig. 1k, the clear spot pattern indicates the single crystalline of Bi_2Se_3 nanoplates, consistent with the FFT pattern calculated from the HRTEM image. Furthermore, the ring pattern of Bi_2S_3 is obtained from a bundle of nanowires with distinct lattice point orientations (Fig. 1l), which can be fitted in accordance with single Bi_2S_3 nanowire in the inset of Fig. 1i. The heterointerface of Bi_2S_3/Bi_2Se_3 vdWHs is demonstrated by the vertical view of the HRTEM image (Fig. 1g), indicating the d-spacing of

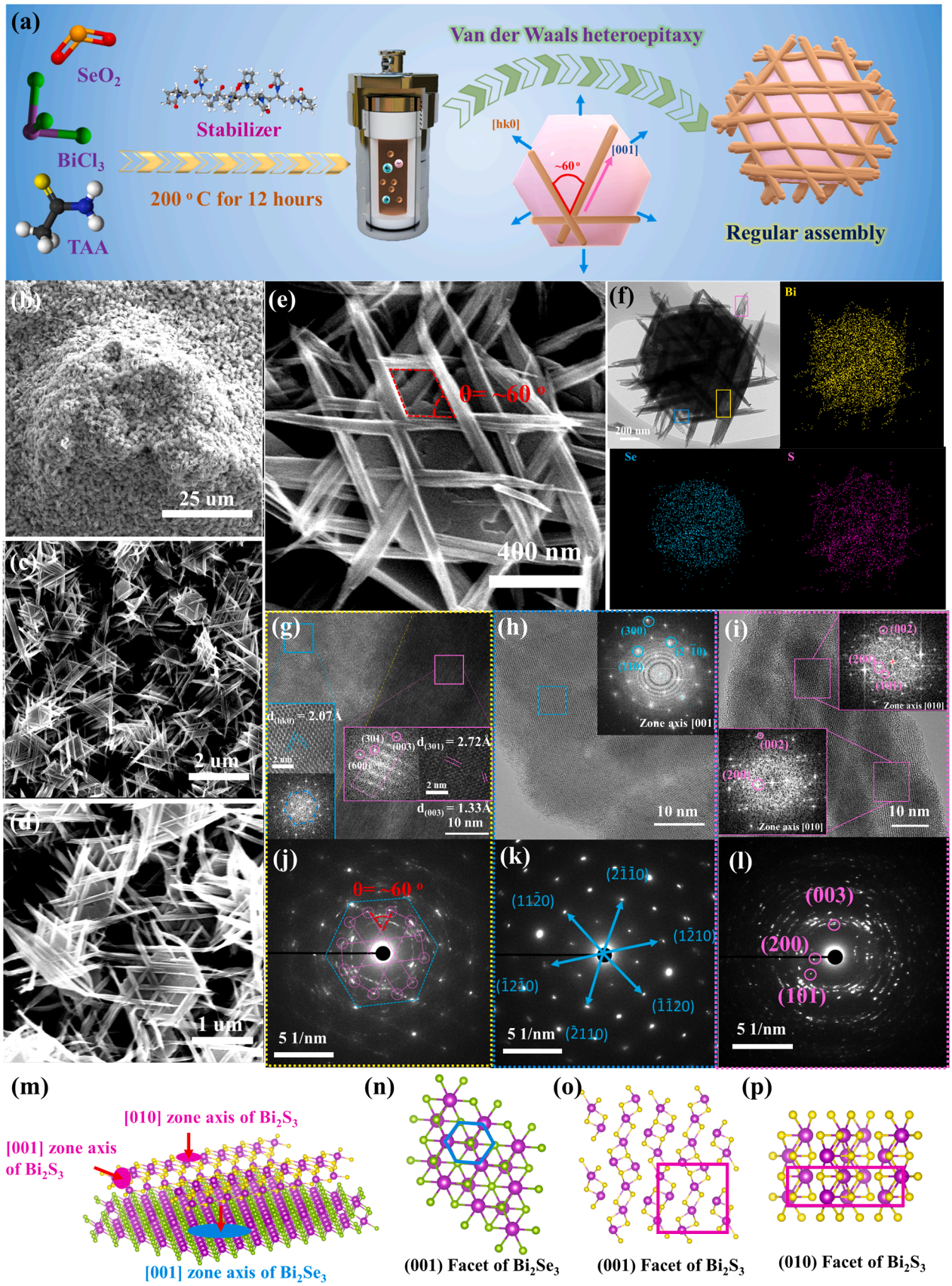

Fig. 1. (a) Schematic illustration of the fabrication of Bi_2S_3/Bi_2Se_3 vdWHs. Morphology characterization in (b–d) low-magnification and (e) high-magnification SEM images of Bi_2S_3/Bi_2Se_3 vdWHs. The high-magnification TEM image and corresponding EDS elements mapping of a Bi_2S_3/Bi_2Se_3 vdWHs. The lattice fringes and spacing in HRTEM analysis and SAED pattern of (f, i) heterointerface, (g, j) (001)-orientated Bi_2Se_3, (h, k) (010)-orientated Bi_2S_3. (m-p) schematic diagrams of oriented planes and their relationship between facets and zone axis.

(hk0) planes (blue frame, Bi_2Se_3) and (301) and (003) plane (pink frame, Bi_2S_3). In addition, the FFT pattern of Bi_2S_3 and Bi_2Se_3 in heterostructure shows the rectangular and hexagonal dash shape, respectively, which is reasonable for the crystal family viewed from the [010]-direction of Bi_2S_3 and [001]-direction of Bi_2Se_3. As shown in Fig. 1j, the SAED pattern of Bi_2S_3/Bi_2Se_3 vdWHs displays the six symmetry directions of equivalence in Bi_2Se_3 lattice system, while the regular assembly of Bi_2S_3 nanowires follows the [hk0]-oriented Bi_2Se_3 nanoplates along six directions with intersection angle of 60°. To more clearly present the exposed lattice planes in Bi_2S_3/Bi_2Se_3 vdWHs, the schematic in Fig. 1m shows different zone axes, illustrating that the exposed faces perpendicular to the zone axis [hkl] belong to (hkl) planes, based on the Bragg law. Both FFT and SAED patterns of vdWHs can indicate the related orientations and facets of Bi_2S_3 and Bi_2Se_3, in accordance with crystal shape of corresponding lattice spots in a unit cell. The hexagram lattice points of the (001) facet of rhombohedral Bi_2Se_3 is consistent with the atomic arrangement of unit cell in blue region of Fig. 1m and n. Meanwhile, the (001) and (010) facets of Bi_2S_3 in cross-section plane and side plane of nanowires demonstrate the square and rectangular shape of unit cell in pink region of Fig. 1o and p, respectively. The above-mentioned d-spacing data measured from the Gatan software are given in Figs. S10–S12. Therefore, the small mismatch between the lattice constants of c-axis for orthorhombic Bi_2S_3 and the a- and b-axis for the rhombohedral Bi_2Se_3 (detailed lattice constant in Table S1) can be responsible for the preferential growth of [001]-oriented Bi_2S_3 nanowire on the (001)-exposed plane of hexagram Bi_2Se_3 nanoplates along the [2-10], [1-20], [110], [-1-10], [-120], and [-210] directions.

We perform density functional theory (DFT) calculations to gain insight into the atomic dimensions of the heterointerface between rhombohedral Bi_2Se_3 and orthogonal Bi_2S_3. As shown in **Fig. 2a**, there is

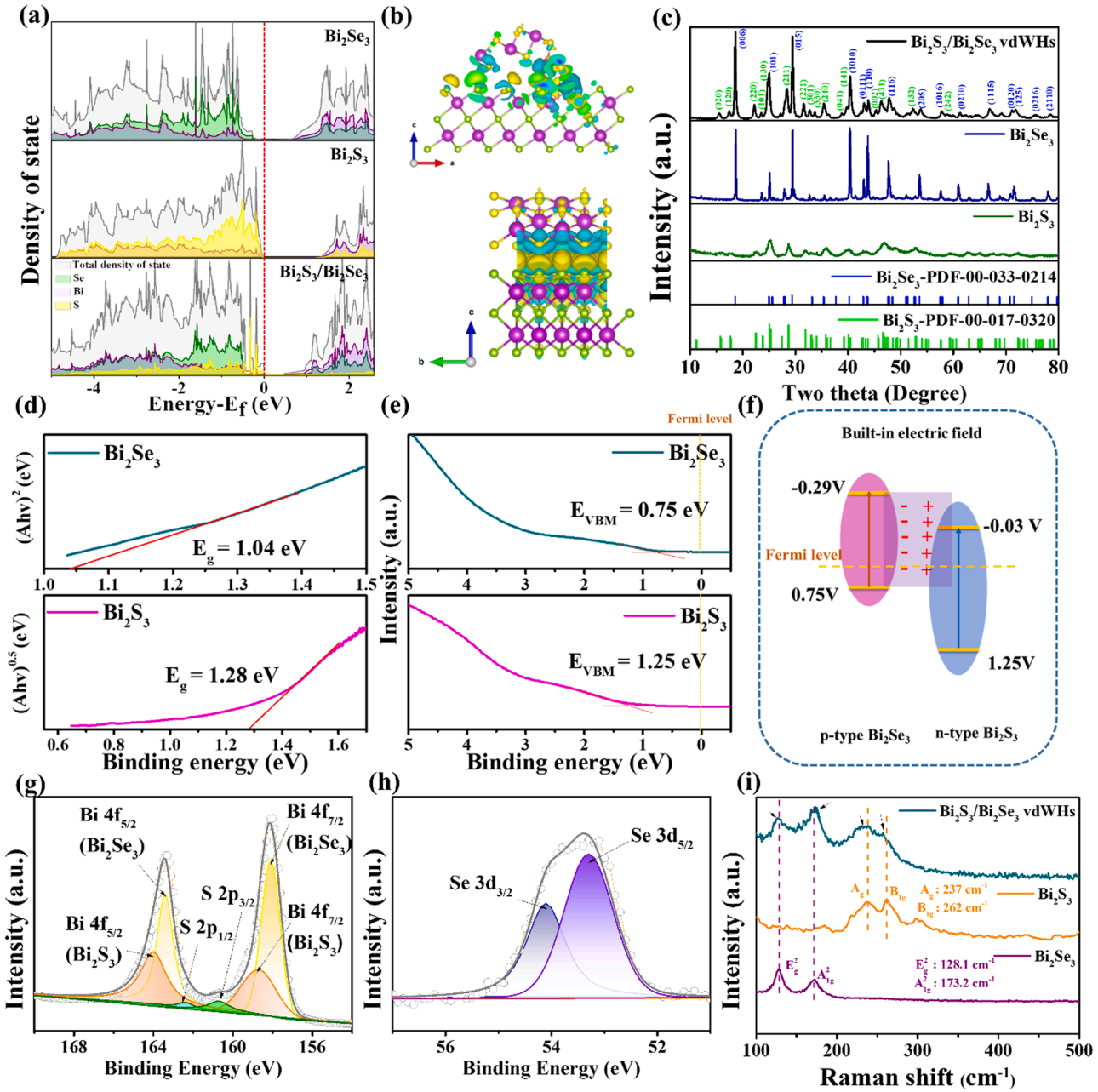

Fig. 2. (a) Calculated density of state (DOS) analyses and (b) charge density difference for Bi_2S_3/Bi_2Se_3 vdWHs. (d) UPS valence band spectra of Bi_2Se_3 and Bi_2S_3. (e) Tauc's bandgap plots. (f) Band diagram for p-type Bi_2Se_3 and n-type Bi_2S_3. Material characterization in (c) XRD pattern, high-resolution XPS spectrum of (g) Bi 4f and S 2p, and (h) Se 3d region. (i) The Raman spectrum of Bi_2S_3/Bi_2Se_3 vdWHs, Bi_2S_3 nanowires, Bi_2Se_3 nanoplates.

a narrow bandgap in Bi_2Se_3 owing to the topological effect, while the Bi_2S_3 exhibit a larger bandgap of 1.23 eV. When the vdWHs is obtained, the bandgap shows an offset near the Fermi level with lager contribution of density of state (DOS) intensity, indicating the optimized electrical conductivity compared to pure Bi_2S_3 and Bi_2Se_3. Based on the DOS result of Bi_2Se_3 and Bi_2S_3, the p-n junction of heterostructure is formed due to the built-in electric field, enhancing the charge transfer between two materials (Fig. S9) [37,38]. Moreover, point-contact and line-contact heterostructures can only provide few hetero boundaries, while planar contacts can provide high surface contact boundaries. However, it is difficult to diffuse K^+ from the top surface to the inner surface. Compared to point-contact, line-contact and plane-contact heterostructures, the rich network-contacted hetero-boundaries can facilitate ordered ion/electron transport around the surface network and interior topological materials, and simultaneously promoting the K^+ diffusion, electron transfer, and electrolyte infiltration from the top surface of Bi_2S_3 network to heterointerface of Bi_2Se_3. The 1D Bi_2S_3 and 2D Bi_2Se_3 crystal structure with (010) facet and (001) facets are used to simulate the charge density difference of vdWHs in Fig. 2b. The deformation of charge density reveals the distribution of electrons in depletion (green) and accumulation (yellow), confirming the direction of electron contribution and transportation [39]. Most of the charges in vdWHs are concentrated around mainly Se atoms and partly S atoms, and the dissipated parts are located in the sublayer of Bi atoms and interface of Bi_2S_3 and Bi_2Se_3. Significant charge transfer is constructed from Bi_2Se_3 to Bi_2S_3 to facilitate electron transfer to the metal layer and forming an electron transport route [40]. Moreover, the purity and element composition of Bi_2S_3/Bi_2Se_3 vdWHs, Bi_2S_3 nanowires, Bi_2Se_3 nanoplates are confirmed using X-ray diffraction (XRD) technique and X-ray photoelectron spectroscopy (XPS). All the diffraction peaks of Bi_2S_3/Bi_2Se_3 vdWHs well-matched with rhombohedron Bi_2Se_3 (R-3m (166), JCPDS No. 00-033-0214) and orthorhombic Bi_2S_3 (Pbnm (62), JCPDS No. 00-017-0320) prove the coexistence of Bi_2Se_3 and Bi_2S_3 in the heterostructure (Fig. 2c). There are no obvious impurity peaks appeared in XRD pattern. Based on the ultraviolet–visible (UV–vis) spectra, the bandgap of the Bi_2Se_3 (direct semiconductor) and Bi_2S_3 (indirect semiconductor) estimated according to the Tauc's method are 1.04 and 1.28 eV (Fig. 2d). In addition, the absorption spectrum of direct band gap materials should be able to distinguish intrinsic absorption band and absorption edge more clearly, the change is relatively slow, but that for indirect band gap materials is steep [41,42]. To further confirm the semiconductor type and p-n heterojunction, ultraviolet photoelectron spectroscopy (UPS) of Bi_2Se_3 and Bi_2S_3 are performed to investigate the electron band configuration. As displayed in Fig. 2e, the valence band maximum (VBM) edges for Bi_2Se_3 and Bi_2S_3 are 0.75 and 1.25 eV, respectively. Because of the different Fermi level positions, spontaneous electron transfer occurs during contact, leading to the formation of a built-in electric field. Accordingly, the energy band diagram is illustrated in Fig. 2f, with a spontaneous built-in electric field formation when the p-type Bi_2Se_3 and the n-type Bi_2S_3 are in contact. This induces the direct migration of electron and K ions between Bi_2Se_3 and Bi_2S_3, realizing a spatially optimized distribution of charged species. Besides, the full XPS survey spectra of Bi_2S_3/Bi_2Se_3 confirm the elemental existence of Bi, Se, and S in Fig. S13. The Bi 4f spectrum (Fig. 2g) demonstrate the 4f core splitting into Bi $4f_{5/2}$ and Bi $4f_{7/2}$ with binding energies of 164.0 and 158.7 eV, 163.4 and 158.1 eV corresponding to Bi (III) in Bi_2S_3 and Bi_2Se_3, respectively [43,44]. In the S 2p spectrum overlapped with Bi 4f, the characteristic peaks at 162.4 and 161.0 eV can be distinguished as S $2p_{1/2}$ and S $2p_{3/2}$ [45]. The peaks in Fig. 2h at 54.1 eV (Se $3d_{3/2}$) and 53.3 eV (Se $3d_{5/2}$) can be considered as the formation of a Bi-Se bond [46]. In addition to compound distribution, there are properties deduced from Raman spectra, such as peak width, peak intensity, peak shift, and peak polarization state [47–50]. Among them, the peak shift can further identify the change of stress and strain states caused by heterostructure formation. In the as-prepared Bi_2Se_3 and Bi_2S_3, the out-of-plane mode A_g^2 (173.2 cm^{-1}) and in-plane mode E_g^2 (128.1 cm^{-1}) of Bi_2Se_3 as well as A_g (237 cm^{-1}) and B_{1g} (262 cm^{-1}) of Bi_2S_3 are demonstrated in Fig. 2i. [51,52] and schematic vibrational modes displayed in Fig. S14. [53] The Raman spectroscopy was employed to characterize the formation of 1D/2D vdWHs. Compared to the individual materials, the Raman spectrum of Bi_2S_3/Bi_2Se_3 vdWHs reveals the peak positions of E_g^2, A_g^2, A_g, and B_{1g} at 126.4, 175.6, 230.8 and 257.2 cm^{-1}, indicating the slight blue shift of A_g^2 and red shift of E_g^2, B_{1g}, and A_g vibration modes. If compressive stress is applied in the crystal, the bond lengths in the crystal will shorten relative to their original length in the unstressed crystal, causing the Raman peak positions to shift to higher frequencies. Conversely, if there is tensile stress in the crystal lattice, and the chemical bonds are elongated relative to their normal position in an unstressed crystal. As the bond length increases, while the force constant remains constant, a decrease in vibrational frequency and a red shift is expected [54]. Besides, the limited surface reaction of viscous solvent and PVP surfactant, the vdW assembly of Bi_2S_3 on the (001) facet of Bi_2Se_3 restrains the growth of nanoplate thickness, resulting in preferential growth towards the [hk0] direction of Bi_2Se_3. Therefore, the in-plane E_g^2 mode develops a slight redshift of 1.7 cm^{-1}, while the out-of-plane mode A_g^2 presents a blueshift of 2.4 cm^{-1}. Likewise, the redshift of B_{1g}, and A_g vibration modes in Bi_2S_3 are affected by van der Waals contact with Bi_2Se_3 nanoplates and other Bi_2S_3 nanowires [55], suggesting anisotropic phonon vibrations owing to low symmetry of Bi_2S_3 crystal structure [56]. These results indicate that the process of heteroepitaxial growth of Bi_2S_3 on Bi_2Se_3 is under significant in-plane tensile strain and strong out-of-plane vdW contact, attributing to the charge transfer and lattice change between Bi_2S_3 and Bi_2Se_3 [57,58]. As a consequence, Raman results illustrate the successful construction of the vdWHs consisting of 1D Bi_2S_3 nanowires and 2D Bi_2Se_3 nanoplates rather than formation of $Bi_xSe_yS_z$ compound.

2.2. Electrochemical tests and analysis

The electrochemical performance of Bi_2S_3/Bi_2Se_3 vdWHs was evaluated by assembling coin-type half cells. The specific capacity directly reflects the utilization efficiency of conversion products (e.g., K_2S and K_2Se), while the cycling retention can embody the ability to inhibit the shuttle effect [24]. As cycled after 50 times at a low current density of 50 mA g^{-1}, the severe capacity decay of Bi_2Se_3 (182.9 mA h g^{-1}) and Bi_2S_3 (269.1 mA h g^{-1}) were obtained in **Fig. 3a**. In addition, hybrid materials fabricated by mixing Bi_2S_3 nanowires and Bi_2Se_3 nanoplates *via* ultrasonic dispersion, namely M-BSS, performed as poor as the inherent properties of Bi_2Se_3 and Bi_2S_3. Noticeably, the Bi_2S_3/Bi_2Se_3 vdWHs delivers a better retention with a charge capacity of ~430 mAh g^{-1} after 50 cycles, in contrast to the other materials in this work. The galvanostatic charge-discharge (GCD) curves of the 1st and 50th cycle are shown in Fig. 3b. The first plateau at 1.8~1.5 V (blue frame) and the second plateau at 1.0~0.6 V (pink frame) correspond to formation of solid-electrolyte-interface (SEI) layer and multiple conversion reaction, respectively (Fig. 3c). Except for Bi_2S_3 nanowires with higher overpotentials, the other three anode materials exhibit the similar overpotentials, indicating the smaller charge transfer resistance (Rct) during the solid-liquid phase transition. However, the longer SEI layer growth time on Bi_2Se_3 means more electrolyte consumption and the formation of a thicker SEI layer compared to other materials [59]. During the process of a conversion reaction, the low polarization and long plateau of GCD curves of Bi_2S_3/Bi_2Se_3 vdWHs mean the better reaction kinetics and K_2S/K_2Se utilization. Although Bi_2S_3 nanowire anodes deliver a higher initial discharge capacity than Bi_2S_3/Bi_2Se_3 vdWHs, their larger overpotentials suggest that electrochemical reactions and K ions will become increasingly difficult to proceed and transfer, which is reflected in the polarization of the GCD curves. For the initial charge state (yellow frame), each anode undergoes the reverse conversion and dealloying reactions. When the charging voltage reaches 1.0 V, the Bi_2S_3/Bi_2Se_3 vdWHs contributes the wide plateau and low polarization conditions. In particular, the reactivity and reversibility of conversion products of

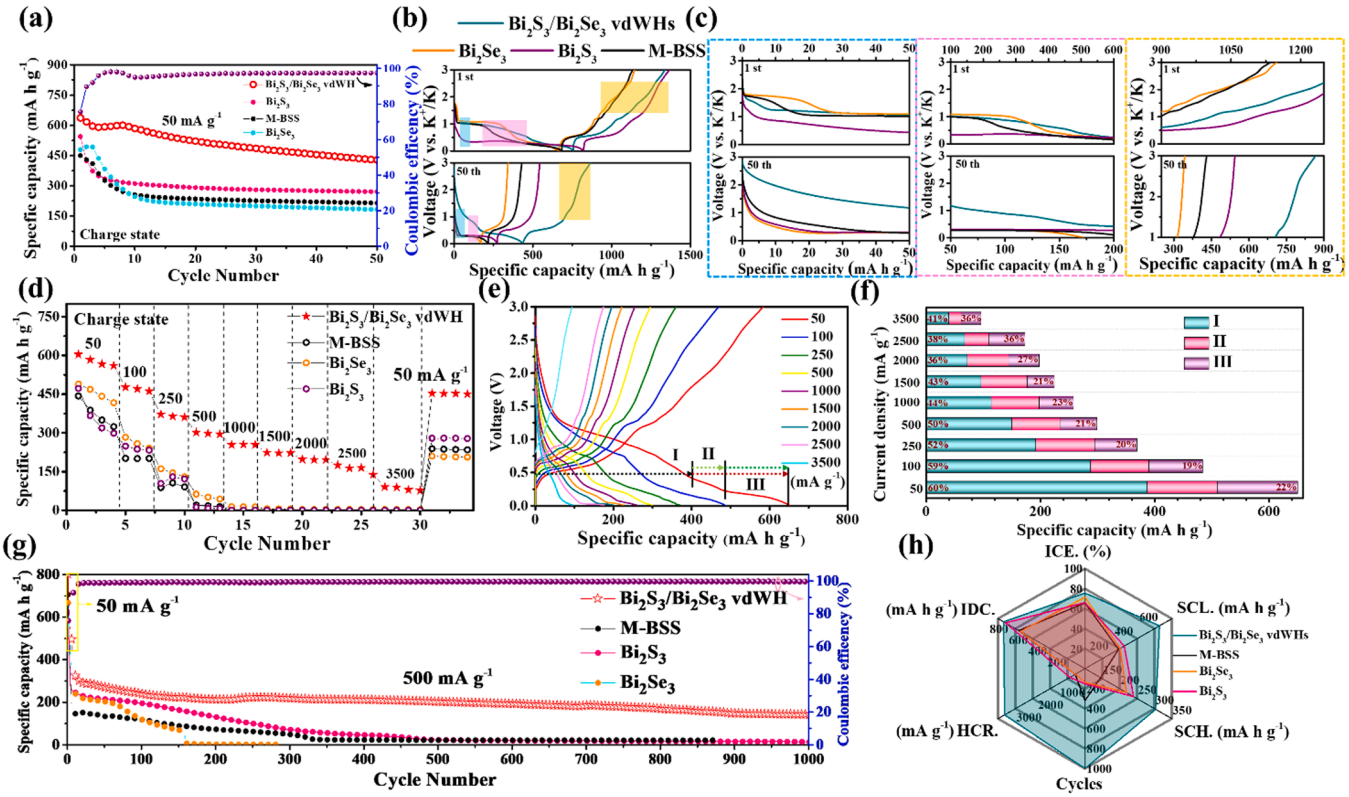

Fig. 3. Electrochemical analysis and performances of Bi_2S_3/Bi_2Se_3 vdWHs in PIB half cells. (a) Cycling performance at a current density of 50 mA g^{-1}. (b) Galvanostatic charge–discharge profiles with the 1st and 50th cycle at 50 mA g^{-1}. Enlarged area of (c) the initial plateau (blue frame) and the second plateau (pink frame) of conversion reaction in discharge state, and plateau in charge state (yellow frame). (d) Rate capability and (e) galvanostatic charge–discharge profiles of Bi_2S_3/Bi_2Se_3 vdWHs at various rates. (f) Discharge capacity from the conversion plateau (denoted as I), first alloying plateau (denoted as II), and second alloying plateau (denoted as III) at different current rates. (g) Long-term cycling stability of Bi_2S_3/Bi_2Se_3 vdWHs at 500 mA g^{-1}. (h) Comparison results of initial Coulombic efficiency (ICE), initial discharged capacity (IDC), highest current rate (HCR), low-rate specific capacity at 50 mA g^{-1} (SCL), high-rate specific capacity at 500 mA g^{-1} (SCH), and cycle number with Bi_2Se_3 nanoplates and Bi_2S_3 nanowires.

Bi_2S_3/Bi_2Se_3 vdWHs are far superior to other materials in both discharged and charged states. Nevertheless, the overpotentials and polarizations of Bi_2Se_3, Bi_2S_3, and M-BSS increased significantly due to severe structural damage and the increased R_{ct}, indicates that K ions are difficult to diffuse into the materials after 50 cycles of activation. Furthermore, the discharge and charge plateau of conversion reaction at ~1.0 V and 2.5 V, respectively, are gradually disappeared, implying the irreversibility of conversion reaction in Bi_2Se_3, Bi_2S_3, and M-BSS. In addition, Bi_2S_3/Bi_2Se_3 vdWHs greatly enhance the reversibility and cyclability of the anode due to the entrapment capability and volume change mitigation during cycling. The rate capability of anode materials was evaluated from 0.1C to 7C (1C = 500 mA g^{-1}) to demonstrate the positive effect of vdWHs on conversion kinetics in Fig. 3d. At stepwise current densities, the excellent rate performance of Bi_2S_3/Bi_2Se_3 vdWHs is marked as 604, 477, 372, 302, 255, 221, 196, 175, and 89 mAh g^{-1} at 50, 100, 250, 500, 1000, 1500, 2000, 2500, and 3500 mA g^{-1}, respectively. Compared with the host material, the capacities of Bi_2S_3, Bi_2Se_3, and M-BSS were continuously decreased, and the capacity contributions of the three materials under high-rate conditions are negligible. The GCD curves of rate performance (Fig. 3e) can be classified into three plateaus correspond to the conversion reaction (I) (theoretical capacity of K_2S and K_2Se: 1675 and 678 mA h g^{-1}), KBi_2 formation of alloying reaction (II) (theoretical capacity of transformation of KBi_2: 64 mA h g^{-1}), and K_3Bi formation of alloying reaction (III) (theoretical capacity of transformation of KBi_2 to K_3Bi: 322 mA h g^{-1}). Despite capacity fading with increasing current rate owing to the insufficient reduction of polysulfide and polyselenide, the plateau I still provides an approximately 40 % of the discharge capacity at a significantly high current density of 3500 mA g^{-1} (Fig. 3f). Therefore, we believe that benefiting from more active sites providing continuous diffusion paths for ions and electrons, this can contribute to improved K^+ storage capacity and better migration in vdWs assembled structures. Effective charge carriers in electrochemical reactions help to reduce polarization caused by changes in current. Long-term cyclability is another significant indicator for evaluating the electrochemical stability and reversibility. The regularly assembly of crosslinked Bi_2S_3 nanowires with 2D Bi_2Se_3 nanoplates strengthens the van der Waals interaction in the heterojunction, and effectively enhanced the structural stability of the anodes without assistance of carbonaceous materials. Besides, the cycling performance of different S/Se molar ratio of heterostructure are displayed in Fig. S15. Both regular heterostructures of Bi_2S_3/Bi_2Se_3 ratio of 1:1 and 1:2 ratio can demonstrate a stable long-term cycling performance, but Bi_2S_3/Bi_2Se_3 ratio of 1:1 showed a higher capacity resulted from the higher content of Bi_2S_3. The performance of Bi_2S_3: Bi_2Se_3 ratio of 2:1 and simple mixing of Bi_2S_3 and Bi_2Se_3 (M-BSS, Fig. S2d) rapidly decayed after 100 cycles in Figs. S15 and 3g, respectively. The post-mortem SEM images of Bi_2S_3/Bi_2Se_3 vdWHs demonstrate the good contact even after cycling in Fig. S16a–c. Due to the lack of junction effect and well-crosslink structure, the random-aligned structures cannot effectively improve the intrinsic properties and structural durability, resulting in the rapid decay of cycling performance.

As expected, the Bi_2S_3/Bi_2Se_3 vdWHs delivered a higher reversible capacity of 201.7 mAh g^{-1} (Fig. 3g) at a high current density of 500 mA g^{-1} than other three materials. We compare Bi_2S_3/Bi_2Se_3 vdWHs with other three materials in six aspects, including initial Coulombic efficiency (ICE), initial discharged capacity (IDC), highest current rate (HCR), low-rate specific capacity at 50 mA g^{-1} (SCL), high-rate specific capacity at 500 mA g^{-1} (SCH), and cycle number, are displayed in the

radar chart of Fig. 3h. Because of the inevitable capacity loss inherent from the conversion reaction, the irreversible reaction involved in the initial cycle induces that the ICE of all materials is less than 80%. Bi_2S_3/Bi_2Se_3 vdWHs not only possess appreciable gravimetric capacity at both low current and high current rate, but also achieve cycling capability up to 1000 cycles due to the interconnected diffusion channels of nanowires and the topological surface effect of 2D nanoplates.

The Bi_2S_3/Bi_2Se_3 vdWHs exhibit superior K^+ storage ability and cyclability that are associated with pseudo-capacitance and diffusion behaviors at high and low rates. To verify the advantages of the heterointerface in the PIB system and study its kinetic response, cyclic voltammetry (CV) tests were performed at different scan rates. The CV curves at stepwise sweeping rates from 0.1 mV s^{-1} to 1.0 mV s^{-1} (Figs. 4a and S17) remain unchanged shape of curves, rather than the phase transition of Bi_2S_3, Bi_2Se_3, and M-BSS in Fig. S18. The current is composed of surface-dominated and diffusion-dominated reactions, which can be evaluated by the formula below [60,61]

$$i_p = av^b (b = 0.5 \sim 1.0) \quad (1)$$

where a and b are adjustable constants in power law. Notably, the b value is relatively important as the fitted slope of logarithmic i_p (peak current) and logarithmic v (sweeping rate) shows the kinetic contribution on the surface of electrode. There are four major peaks (C_1, C_2, A_1, A_2) for the cathodic and anodic process, and their corresponding b values are 0.69, 0.91, 0.84, and 0.62, respectively (Fig. 4b). Thus, it was initially determined that the Faraday and Faraday processes would simultaneously contribute to the current in the K^+ reservoir. Furthermore, the green and purple frame are assigned to the conversion and alloying reaction, respectively. The b values indicated the different capacity contribution type of each electrochemical reaction. Therefore, b values of cathodic and anodic peaks are divided into two couple of redox reaction peaks, which could be indexed to the conversion (C1 and A2) and alloying reaction (C2 and A1). Due to their same electrochemical reaction, the similar b value of each couple of peaks can indicate the similar capacity contribution type. According to the Figs. 4 and 3f, the conversion reactions (C1 and A2 peaks) were predominated by diffusion-controlled ($b < 0.75$), meaning that it could provide complete reactions at low current rate, but cannot contribute same capacity contribution ratio (%) at high-rate cycling process. The alloying reactions (C2 and A1 peaks) were capacitance-controlled type ($b > 0.75$), in contrast to the conversion reaction, with a higher capacity contribution (%) at high current densities. We further employ scan rate-dependent CV curves to explore and quantify the contribution of capacitive effects, including pseudo-electric double-layer capacitance and double-layer capacitance, as well as diffusion-controlled K^+ insertion. Relational equations are used for calculation.

$$i = k_1 v + k_2 v^{0.5} \quad (2)$$

$$i/v^{0.5} = k_1 v^{0.5} + k_2 \quad (3)$$

The k_1 v stands for the non-faradaic reaction, and k_2 $v^{0.5}$ represents the faradaic reaction. By plotting i(V)/ $v^{0.5}$ and $v^{0.5}$ at specific range of potentials, a linear fitting for the slope of k_1 and intercept of k_2 can be calculated and achieved from the Eq. (3) and Fig. S19. This allows quantification of the reaction current for capacitive and diffusive contribution at a given potential of A_1 and C_1 peaks. A closed region of CV curve at 1.0 mV s^{-1} are shown in Fig. 4c, the percentage of capacitive contribution relative to the total area is 65.6% at 1.0 mV s^{-1}. Namely, the capacitance-controlled current is slightly larger than diffusion-controlled current within the inner surface, indicating that the high-rate performance can be benefit by partly contribution of surface capacitance. Additionally, capacitive percentages of 42.8, 45.9, 44.7, 52.6, 57.9, and 65.6% are given in Figs. 4d and S20 from the integrated area for the sweeping rates of 0.1, 0.2, 0.4, 0.6, 0.8, and 1.0 mV s^{-1}, respectively. To prove the important existence of heterointerface, the galvanostatic intermittent titration technique (GITT) and operando electrochemical impedance spectroscopy (EIS) are carried out to measure the diffusion coefficient of K^+ (D_{K+}) and R_{ct} in Fig. 4g–i. The D_{K+} of Bi_2S_3/Bi_2Se_3 vdWHs and M-BSS are calculated from GITT curves based

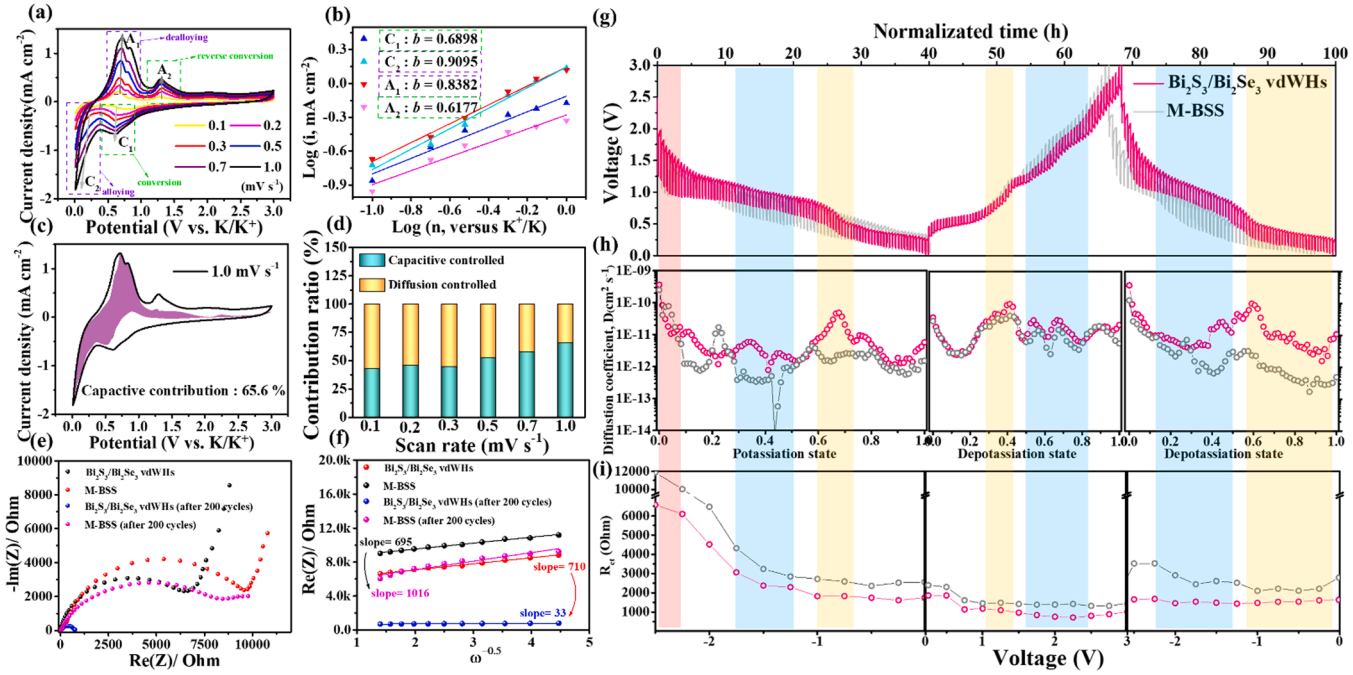

Fig. 4. Kinetics analyses of the K^+ storage behaviors for Bi_2S_3/Bi_2Se_3 vdWHs electrode. (a) CV curves of Bi_2S_3/Bi_2Se_3 vdWHs at different sweeping rates. (b) The corresponding b values in linear regression. (c) The composition of pseudocapacitive characteristics in the CV curve at a scan rate of 1.0 mV s^{-1}. (d) The contribution ratio of surface-controlled and diffusion-controlled behaviors at different scan rates. (e) Nyquist plots of Bi_2S_3/Bi_2Se_3 vdWHs and Bi_2Se_3+Bi_2S_3 before and after cycling test. (f) Linear diagram of impedance and frequency components in (e). (g) GITT curves with 10 min current pulse of 50 mA g^{-1} followed by 30 mins relaxation and (h) corresponding diffusion coefficients of each current pulse. (i) Variation of Charge-transfer resistance in *in situ* EIS at 50 mA g^{-1}.

on the simplified Eq. (4) [62,63].

$$D = \frac{4}{\pi\tau}L^2\left(\frac{\Delta E_s}{\Delta E_t}\right)^2 \quad (4)$$

where τ, ΔE_s, ΔE_t, and L are denoted as current pulse time (s), constant voltage change caused by the current pulse, potential change in the steady-state current pulse, and thickness of electrode, respectively, which is determined by cross-section SEM image in Fig. S21. As shown in Fig. 5h, the diffusivity of M-BSS severely fluctuates around 10^{-10}~10^{-15} $cm^2\ s^{-1}$ during the potassiation state, while the Bi_2S_3/Bi_2Se_3 vdWHs can display the stable tendency of diffusivity in the smaller range between 10^{-10} and 10^{-11} $cm^2\ s^{-1}$. It is worth mentioning that the insertion of large potassium ions leads to structural deformation and destruction, leading to gradually detaches from the electrode during subsequent cycling. The obvious decreased D_{K+} can be presented in the potassiation state of second cycle in M-BSS. Meanwhile, the regularly assembled Bi_2S_3/Bi_2Se_3 vdWHs effectively avoid the above phenomenon. Consistent with the results and trend of GITT tests, the *in-situ* EIS demonstrates the continuous variation of R_{ct} during the charge-discharge state given in Figs. 4i, and S22–S23. The R_{ct} of Bi_2S_3/Bi_2Se_3 vdWHs is one-half and even one-third that of M-BSS during the cycling process. Furthermore, the Warburg factors (σ) of both pristine Bi_2S_3/Bi_2Se_3 vdWHs and M-BSS show similar values of 710 and 695 calculated from the slope of the Nyquist plot of Re(Z) and $\omega^{-0.5}$ in diffusion-controlled region, which is located in the low frequency region (Fig. 4e and f). The Bi_2S_3/Bi_2Se_3 vdWHs anode has much smaller R_{ct} (754 Ohms) and Warburg impedance (σ = 33) than the M-BSS anode (R_{ct} = 9202 Ohms, σ = 1016) after 200 cycles. Both operando and *ex-situ* EIS spectrums can prove the significantly reduced barrier of charge transfer and diffusion during the potassiation/depotassiation, suggesting the good conductivity and volume buffering of the vdWHs, stemming from the construction of heterostructure. Therefore, the Bi_2S_3/Bi_2Se_3 vdWHs electrode gives rise to an enhanced charge transfer process, *i.e.*, cycling stability and reversible capacity.

2.3. DFT calculations

To get a deep insight into the impacts of constructed heterointerface on the reaction kinetics, we performed DFT calculations to investigate the adsorption energies and inner diffusion barriers of heterostructured existence with respect to the K^+ storages. The adsorption ability and atomic configurations of heterointerface between 1D Bi_2S_3 and 2D Bi_2Se_3 to the K_2S, K_2Se, and K^+, are demoted and demonstrated in Figs. 5a–c, S24–S25. To simplify the theoretical simulation, Bi_2S_3 (010) plane and Bi_2Se_3 (001) plane are selected to construct Bi_2S_3/Bi_2Se_3 vdWHs based on the observation and results of the HRTEM images and FFT patterns. As a result, the adsorption ability of the heterostructure is greater than that of single Bi_2S_3 and Bi_2Se_3 (Fig. 5d), indicating that the

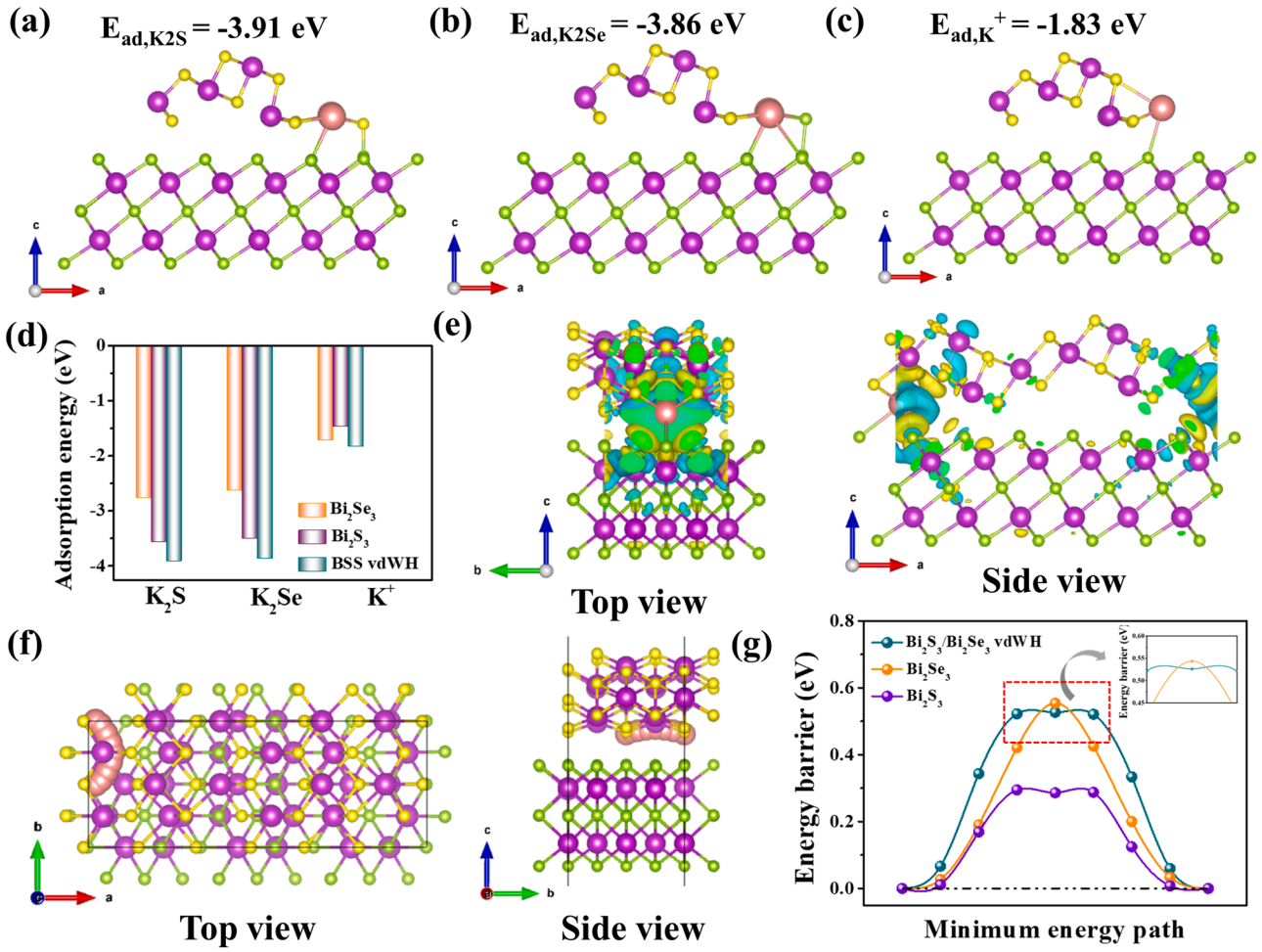

Fig. 5. Theoretical simulation of K^+ adsorption and diffusion between heterointerface. The structural models of possible adsorption sites with (a) K_2S, (b) K_2Se, and (c) K ions adsorption energy on the heterointerface. (d) Comparison of adsorption ability of Bi_2S_3/Bi_2Se_3 vdWHs, Bi_2Se_3, Bi_2S_3 for K_2S, K_2Se, K ions. (e) Differential charge density analysis of Bi_2S_3/Bi_2Se_3 vdWHs with the adsorption of K ions. The yellow and blue surfaces are represented as electron accumulation and depletion, respectively. (f) Energy barrier and diffusion path in top view and side for heterostructure. (g) Comparison of energy barrier of K^+ diffusion in Bi_2S_3/Bi_2Se_3 vdWHs, Bi_2Se_3, Bi_2S_3.

heterojunction effectively suppresses the loss of active materials and the trapping of K ions, thereby promoting the subsequent conversion reactions. Additionally, the deformation of the charge density reveals the dispersion and possible transport direction of electrons in depletion and accumulation, displaying that most of charges and the dissipated region in heterostructure are concentrated around Se and S atoms, and K and Bi atoms (Fig. 5e), respectively. The directional distribution of charges makes electrons easily transferred to the metal layer of heterostructure and assign a charge transfer path during the diffusion of K^+ into the interlayer between the Bi_2S_3 and Bi_2Se_3. When K^+ diffuses into the material, the adsorption of K^+ on stable sites at the heterointerface occurs first, and then K^+ begins to undergo conversion and alloying reactions with the anode material. In order to investigate the diffusion barrier of heterointerface rather than the top surface of two materials, the DFT simulation was conducted on the inner diffusion of three materials. Thus, the adsorption sites of Bi_2S_3, Bi_2Se_3, and vdWHs were calculated as shown in Figs. S26–S28, and the most stable site was selected to further simulate the diffusion paths and barriers in PIBs (Figs. 5f and S29–S31). As shown in Fig. 5g, the Bi_2Se_3 and Bi_2S_3 exhibit the highest and lowest energy barrier of K ions, respectively. Noticeably, the construction of well-diffusion Bi_2S_3 network and electrically conductive Bi_2Se_3 benefit the synergetic effect regarding to different features of dimensions and material properties. Due to the combination of Bi_2S_3 and Bi_2Se_3, the Bi_2S_3/Bi_2Se_3 vdWHs display a suitable and reasonable diffusion barrier under the situation of good entrapment ability. As a consequence, the construction of Bi_2S_3/Bi_2Se_3 vdWHs not only significantly promotes the adsorption of intermediates and diffusion of K^+, but also greatly improves the charge transfer and ion diffusion during the cycling process.

2.4. Reaction mechanism and features of Bi_2S_3/Bi_2Se_3 vdWHs

Apart from exploring the dynamics of K^+, the *operando* and *ex-situ* techniques were used to confirm and reveal the reversible reaction mechanism of Bi_2S_3/Bi_2Se_3 vdWHs. The operando contour plot in the selected two-theta range, stacked along with the charge-discharge profile, interprets the electrochemical evolution of host material during the initial eight cycles in different states. The XRD peaks at 18.6°, 29.4° belong to Bi_2Se_3, while the diffraction peaks of Bi_2S_3 are located at 15.8°, 22.4°, 24.9°, 25.2° and 28.6° before discharge process (Fig. 6a). The peaks of 17.4°, 21.7°, and 24.1°that consistently appear in the contour plot derived from the stainless holder of the *operando* device. When K^+ began to be inserted into the electrode, the open circuit potential (OCP) suddenly dropped to around 1.1 V, starting the first step of the Bi_2S_3/Bi_2Se_3 multiple conversion reactions. The diffraction peaks of the pristine material gradually disappeared, accompanied by 22.3°and 25.8° (JCPDS No. 04-010-8024), 25.7° and 29.8° (JCPDS No. 04-005-3293), which were assigned to the (211) and (220) facet of K_3BiSe_3 as well as the (111) and (200) facet of $KBiS_2$. As the voltage was continuously discharged to 0.75 V, the peaks of K_2Se, K_2S and Bi appear simultaneously at 19.9° and 32.9° (JCPDS No. 00-023-0470), 24.1° and 34.4° (JCPDS No. 01-074-1030), and 27.2° (JCPDS No. 00-044-1246), respectively. Notably, the low-crystalline K_2S and K_2Se can be confirmed by *operando* and *ex-situ* Raman spectrum (Figs. S32 and S33), indicating that the intensive signals of both weak crystalline substances existed at around 131 cm^{-1} and 252 cm^{-1} in the discharge state [64,65]. On account of the formation of Bi metal, the potassiation process can proceed from stage II to stage III, progressively alloying with K^+ and forming the diffraction peaks of KBi_2 at 16.1°, 31.1°, and 32.5° (JCPDS No. 04-010-8776). As the voltage was further discharged to 0.01 V, the characteristic peaks at 18.4°, 28.9°, 29.6° and 34.5° belonging to the (101), (110), (103), and (201) facet of K_3Bi (JCPDS No. 04-003-7091), declaring the completion of the alloying reaction. After the depotassiation process, the diffraction signals of the K_3Bi phase were converted to the KBi_2 phase (stage IV), which then proceeds to dealloy to Bi (stage V). The reverse conversion reaction also continued to form the final phase K_3BiSe_3 and $KBiS_2$, suggesting the Bi_2Se_3 and Bi_2S_3 are irreversible phases in PIBs (stage VI) [66,67]. Therefore, the K^+ at 2nd cycle of conversion reaction reacted with the K_3BiSe_3 and $KBiS_2$ (stage VII). The magnified display of the partial interval in the range of 16°−32° provides clearer evidence to confirm the repetitive characteristic peaks of conversion and alloying intermediates, while the subsequent depotassiation show a similar process to that of the 1st cycle. This result confirms the reversible multistep insertion/extraction mechanism of K^+ based on the conversion-alloying dual mechanism (Fig. 6b). Moreover, the composition of product at discharge and charge states can also be verified *via ex-situ* XPS spectrum. As shown in Fig. 6c, d (full survey XPS spectrum in Fig. S34), the binding energies of NSO_2^-, SO_2F^- and SO_3^- functional groups originating from the electrolyte can be detected [68]. As discharged to 0.01 V in Fig. 6c, the two pairs of doublet peaks of Bi^0 4f and Bi^{3+} 4f with binding energy of 162.9 and 157.8 eV, 164.1 and 159.0 eV, respectively, are associated with the formation of K_3Bi alloy and surface oxidation of electrode, while the 161.2 and 162.0 eV of S 2p correspond to the K_2S phase. When returned to the fully charged state in Fig. 6d, the intensity of the Bi^0 4f peak decreases slightly, implying that K_3Bi (Bi valence: 0) is mainly transformed into $KBiS_2$ and K_3BiSe_3 (Bi valence: 3^+) with a small amount of Bi metal (Bi valence: 0). The slightly deviated peaks of S 2p at 161.3 and 162.1 eV indicate the existence of $KBiS_2$ due to the electronegativity (EN) of Bi^{3+}. The position of the binding energy of an element depends on the oxidation state of the element and the local chemical environment. In the case of inserting a sample by adding another element, if the EN of the inserted element is higher than the base element, the electron density around the base element decreases and the binding energy increases. Conversely, if the EN of the inserted element is lower than the base element, the electron density around it increases and the binding energy decreases, leading to a red shift in binding energy position [69].

The visual morphology and phase evaluation of host material during cycling test are also investigated in Fig. 7. When discharged to 0.6V (Fig. 7a), the post-mortem TEM images display the well-wrapping structure of Bi_2S_3/Bi_2Se_3 vdWHs. The products formed by the conversion and alloying reaction are clearly revealed *via* the SAED pattern (Fig. 7b) and HRTEM image (Fig. 7c), consistent with the results and details of the operando analysis. The crystal lattice fringes of conversion products with the d-spacing of 1.57 and 2.31 Å, 2.6 Å, and 3.28 Å can be assigned to the (422) and (311) plane of K_2Se, the (220) plane of K_2S, and the (012) plane of Bi metal, respectively. The KBi_2 intermediate of alloying reaction have a spacing of 3.36 and 2.38 Å, corresponding to the (220) and (400) phase, respectively. As fully discharged to 0.01 V, the complete alloying reaction are conducted, fitting the related lattice planes of K_3Bi, including the (110), (101), (201), (103) facet with spacings of around 3.09, 4.80, 2.60, and 3.01 Å, respectively (Fig. 7e, f). During the charging process (to 3.0 V), the lattice fringes and spacings of reversible conversion phases (K_3BiSe_3 and $KBiS_2$) are presented in the Fig. 7h, i, and their interplanar distance of 3.09, 2.12, 3.0 Å correspond to the (310), (220), and (200), respectively. Besides, the corresponding databases of KBi_2, K_3Bi, Bi, K_2Se, K_2S, K_3BiSe_3, $KBiS_2$ are attached in Supplementary Table 2. Furthermore, the presence of Bi metal is reasonable for the products of the initial conversion reaction of Bi_2S_3 and Bi_2Se_3. The electrolytes used in the half-cell and operando cell are different due to volatile nature of DMC solvent, which would result in drying of the glass fibers. Therefore, the post-mortem SEM images and corresponding voltage profiles are shown in Figs. S35 and S36. It is worth mentioning that the post-mortem morphology of fully discharge state and charge state (Fig. 7d, g) showed no obvious phase separation of heterostructures. The HAADF image and EDS mapping results of cycled Bi_2S_3/Bi_2Se_3 vdWHs still maintain the heterostructure of Bi_2S_3/Bi_2Se_3 due to the more outer distribution of S element mapping (two red dash-line region in Fig. 7j) than that of Se. Through *operando/ex-situ* XRD, Raman, XPS, TEM analyses, of the cycled vdWHs, the electrochemical evolution is illustrated in Fig. 6e. The proposed mechanism is summarized as follows

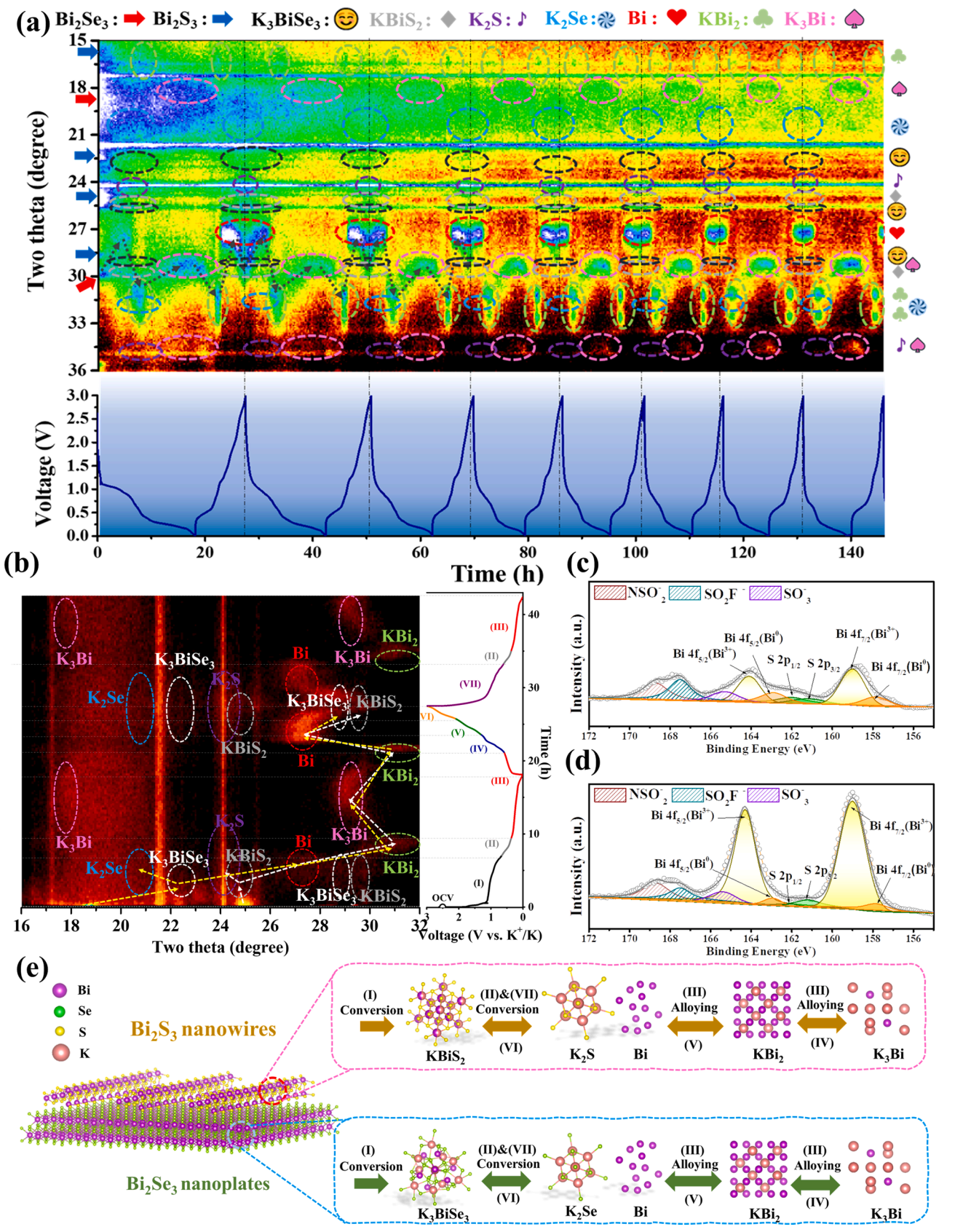

Fig. 6. Analysis of K^+ storage mechanism in Bi_2S_3/Bi_2Se_3 vdWHs. (a) Contour plot of the operando XRD pattern with magnified display ranged from 15 ° to 36 °. (b) The magnified display of the partial interval in the range of 16°-32° during different states of discharge and charge process for initial two cycles. (c, d) XPS spectra of Bi 4f and S 2p after discharging to 0.01 V and charging to 3 V at the initial cycle. (e) Schematic illustration of the K^+ storage mechanism during conversion and alloying reaction.

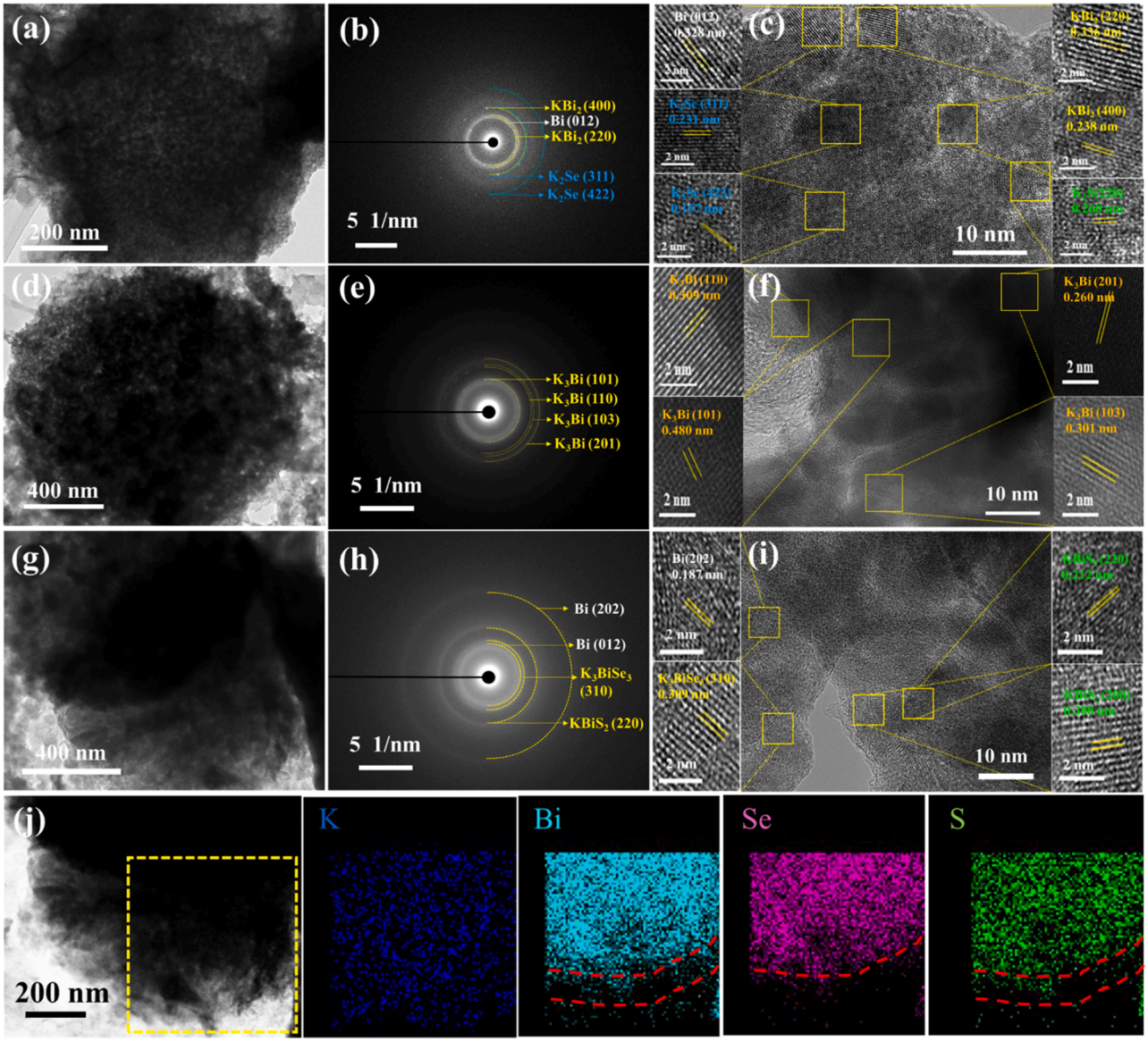

Fig. 7. Post-mortem TEM observations of the cycled Bi_2S_3/Bi_2Se_3 vdWHs. Morphology and HRTEM images with corresponding SAED patterns of Bi_2S_3/Bi_2Se_3 vdWHs: (a–c) discharged to 0.6 V, (d–f) discharged to 0.01 V, and (g–i) charged to 3.0 V. (i) EDS elements mapping of Bi_2S_3/Bi_2Se_3 vdWHs after charging to 3.0 V.

Discharged state

Stage I: $2Bi_2S_3 + 3K^+ + 3e^- \rightarrow 3KBiS_2 + Bi$

$Bi_2Se_3 + 3K^+ + 3e^+ \rightarrow K_3BiSe_3 + Bi$

Stage II&VII: $KBiS_2 + 3K + \ + 3e^- \rightarrow 2Bi + 2K_2S$

$K_3BiSe_3 + 3K^+ + 3e^- \rightarrow 3K_2Se + Bi$

Stage III: $2Bi + K^+ + e^- \rightarrow KBi_2$

$KBi_2 + 5K^+ + 5e^- \rightarrow 2K_3Bi$

Stage IV: $K_3Bi \rightarrow KBi_2 + 5K^+ + 5e^-$

Stage V: $KBi_2 \rightarrow 2Bi + K^+ + e^-$

Stage VI: $2Bi + 2K_2S \rightarrow KBiS_2 + 3K + \ + 3e^-$

$3K_2Se + Bi \rightarrow K_3BiSe_3 + 3K^+ + 3e^-$

The main features of Bi_2S_3/Bi_2Se_3 vdWHs can be attributed to the following aspects: (i) Effective and rational control of kinetic reaction during vdWs epitaxy: the relatively small mismatch between the lattice constants of c-axis for orthorhombic Bi_2S_3 and the a- and b-axis for the rhombohedral Bi_2Se_3 could be responsible for the preferential growth of [001]-orientated Bi_2S_3 nanowire on the top faces of (001)-orientated hexagram Bi_2Se_3 nanoplates along the six symmetry directions of Bi_2Se_3. Therefore, Bi_2S_3 nanowires grew to form interconnected structures, and each bundle of nanowires was aligned in six directions of the 2D Bi_2Se_3 crystal structure. According to Bragg's law, HRTEM images and SAED patterns reveal that the (010) plane of [001]-orientated Bi_2S_3 and the (001) plane of [hk0]-oriented Bi_2Se_3 in vdWHs. We used the two planes for heterojunction simulations. (ii) The built-in electric field induced by the p-n junction between Bi_2Se_3 and Bi_2S_3 accelerates ion/electron diffusion and reduced the activation barrier for electron transfer as demonstrated by EIS and GITT. Based on electron density difference and DOS simulations between the heteroatomic interfaces, a p-n heterojunction with a built-in electric field can be formed to facilitate the charge transfer between Bi_2Se_3 and Bi_2S_3 in the network-contact heterointerface. According to the Raman spectroscopy results, the heterostructure is assembled by vertical vdWs epitaxy, which can effectively avoid lattice mismatch and further alleviate lattice distortion compared with covalently bonded heterophases [70,71]. (iii) The unique architecture effectively ensures the synergetic enhancement of distinct redox plateaus and co-contribution of excellent physical features. Consistent

with the comparison of GCD curves and simulated diffusion and adsorption, the enhanced adsorption energies of K_2S and K_2Se in the heterointerface confirm the excellent cycling ability of Bi_2S_3/Bi_2Se_3 vdWHs. Meanwhile, the adsorption ability and diffusion barrier for K ions must be trade-off to give the optimal value within heterostructure. Under suitable K ions adsorption energy, the electrochemical kinetic diffusion exhibits stable and fast diffusion coefficient and low R_{ct} and diffusion impedance after 200 cycles of charge-discharge procedures. In the operando XRD analysis, the reversible K_3BiSe_3 and $KBiS_2$ phase are revealed and consistently contributed to the greater capacity retention than materials without regular assembly and junction engineering. Due to the robust heterostructure, post-mortem TEM also revealed the existence of a heterointerface with distinct outer and inner distribution of S and Se, respectively, accompanied by reversible phases at each step of electrochemical redox reaction [72–74].

2.5. Potassium-ion full battery and hybrid capacitor

The regularly assembled Bi_2S_3/Bi_2Se_3 vdWHs overcome the intrinsic drawback of individual Bi_2Se_3 and Bi_2S_3 and provide a feasibility for assembling with other cathode materials into full cell systems in PIBs and PIHCs. Due to the high oxidation potential of the conversion products (*e.g.*, K_2S, K_2Se), organic cathodes (*e.g.*, PTCDA) cannot meet high working voltages over 3.5 V. Prussian blue analogs (i.e., KFeHCFs and KMnHCFs) not only cover the voltage range of the anodic conversion reaction, but also maintain excellent cycling performance [75,76]. Hence, Prussian blue nanoparticles, *i.e.*, $K_xFe_2(CN)_6$ (KFeHCF), were used as the cathode material for coupling with Bi_2S_3/Bi_2Se_3 vdWHs in this work. The KFeHCF cathode used in the PIB full cells are synthesized by a co-precipitation method, and all the diffraction peaks of as-prepared material in Fig. S37 are identified [77,78]. The KFeHCF cathode displayed a stable capacity of 63 mA h g^{-1} (Fig. S38). As shown in **Fig. 8a**, the overlapping shape of the CV curves in the PIB full cell initially indicates that the two pairs of redox peaks (1.37/2.86 and 3.07/3.4 V) can be identified with high reversibility. Typical GCD profiles of Bi_2S_3/Bi_2Se_3 vdWHs//KFeHCF full cell in Fig. 8b at current density of 250 mA g^{-1}, based on active mass of cathode with cathode-limited program, show the same values compared to the theoretical capacity of KFeHCF half battery. The relevant plateaus of GCD curve of full cell are consistent with the result of CV profile. Notably, a complete redox reaction of alloying and conversion in the anode provided a considerable specific capacity (blue dash line of Fig. 8b), resulting in different capacity contributions in the anodic or cathodic confined state. The Bi_2S_3/Bi_2Se_3 vdWHs// KFeHCF full cell (Fig. 8c, d) delivers reversible capacities of 91, 80, 64, 56, 52, and 43 mA h g^{-1} at current densities of 50, 125, 250, 500, 1000, and 1250 mA g^{-1}, respectively. When the current density reaches 1250 mA g^{-1}, an obvious overpotential causes a light displacement of plateau. Despite this, due to the high charge-discharge plateaus, Bi_2S_3/Bi_2Se_3 vdWHs//KFeHCF full cell can achieve a high energy density of 208 Wh kg^{-1} and a power

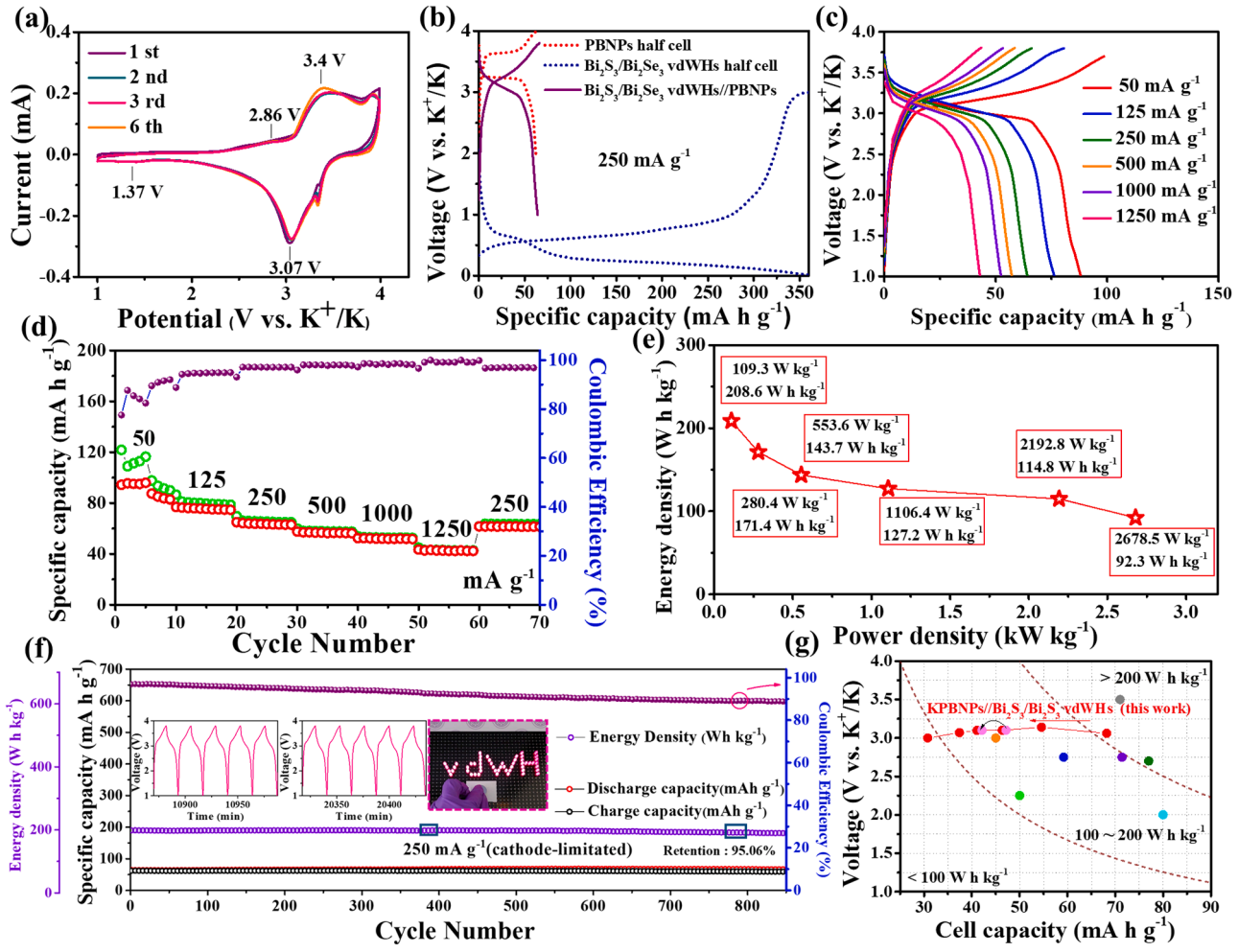

Fig. 8. Electrochemical characteristics of Bi_2S_3/Bi_2Se_3 vdWHs//KFeHCF full cells for K^+ storage in PIBs. (a) The CV profiles at a scan rate of 1 mV s^{-1} and (b) the GCD curves of a half cell and a full cell. (c, d) Rate capability when the current densities is in the range from 50 to 1250 mA g^{-1} and (e) the corresponding energy densities and power densities in Ragone plot. (f) Long-term cycling performance at 250 mA g^{-1}. The inset shows a digital picture of the voltage profiles and lighting test. (g) Comparison of the electrochemical performances pairings with cathode in Prussian blue analogues.

density up to 2678 W kg^{-1} recalculated based on total active materials of both electrodes in Fig. 8e. The calculation equations are followed the usual method for battery system [79]. Furthermore, the long-term cycling performance of Bi_2S_3/Bi_2Se_3 vdWHs//KFeHCF full cell exhibits an ultrastable retention of 88.9% after 850 cycle at current density of 250 mA g^{-1}, with an initial capacity of around 64 mA h g^{-1} (Fig. 8f). The insets of Fig. 9f shows the voltage profiles for 400 cycles and 800 cycles, indicating the high reversibility of potassiation and depotassiation reactions. The lighting test of coin-type full cell is performed by lighting 54 red light-emitting diodes (LED) bulbs with a working voltage of 1.7−2.0 V (Fig. S39). In addition, the energy density of the PIB full cells is compared with that the reported literatures of Prussian blue analogues as cathodes (see Table S3 for detail data) [80–86]. The battery capacities and their voltage window are illustrated in Fig. 8g. We recalculated the rate capacity (red points) and cycling performance (pink points) in the comparison pattern, with red and black arrows indicating different states of current rate increase and initial/final states of cycling tests, respectively. It is noteworthy that the excellent performance of Bi_2S_3/Bi_2Se_3 vdWHs//KFeHCF full cell is in good agreement with the stable contribution of conversion and alloying reaction.

Furthermore, we composed asymmetrical PIHC devices constructed by Bi_2S_3/Bi_2Se_3 vdWHs anode and a commercial activated carbon (AC) cathode to highlight the advantages of heterostructures in electron and K ion transfer capabilities. The operating mechanism of PIHCs is based on the Faradaic reaction of K^+ at the anode and non-faradaic reaction of FSI anion on the cathode [87]. The individual redox peaks of half and full cells in CV curve of **Fig. 9a**. The polarization of CV curve reveals that electrolyte decomposition may occurs when the working voltage is higher 3.8 V. At high cutoff voltage of 0.5-3.9 V, this crucial parameter will increase the energy density and power density considering the integral and covert equation [88].

$$E = C \times V = \frac{I}{m} \int_{t}^{t1} V(t)\, dt = P \times t \tag{5}$$

Note that C, V, I, m, and t are specific capacity, operating voltage, constant current, overall active mass of cathode and anode, and period of discharge, respectively. Obviously, the CV curve of Bi_2S_3/Bi_2Se_3 vdWHs//AC shows a lower polarization shape compared with the sharp redox peaks in Bi_2S_3/Bi_2Se_3 vdWHs half cells, indicating a pseudo-capacitor-like behavior. The GCD profile are given in Fig. 9b, the reasonable displacement of plateaus is consistent with individual cathode and anode at current density of 50 mA g^{-1}. Due to the co-contribution of Faradaic and non-Faradaic behavior, the voltage

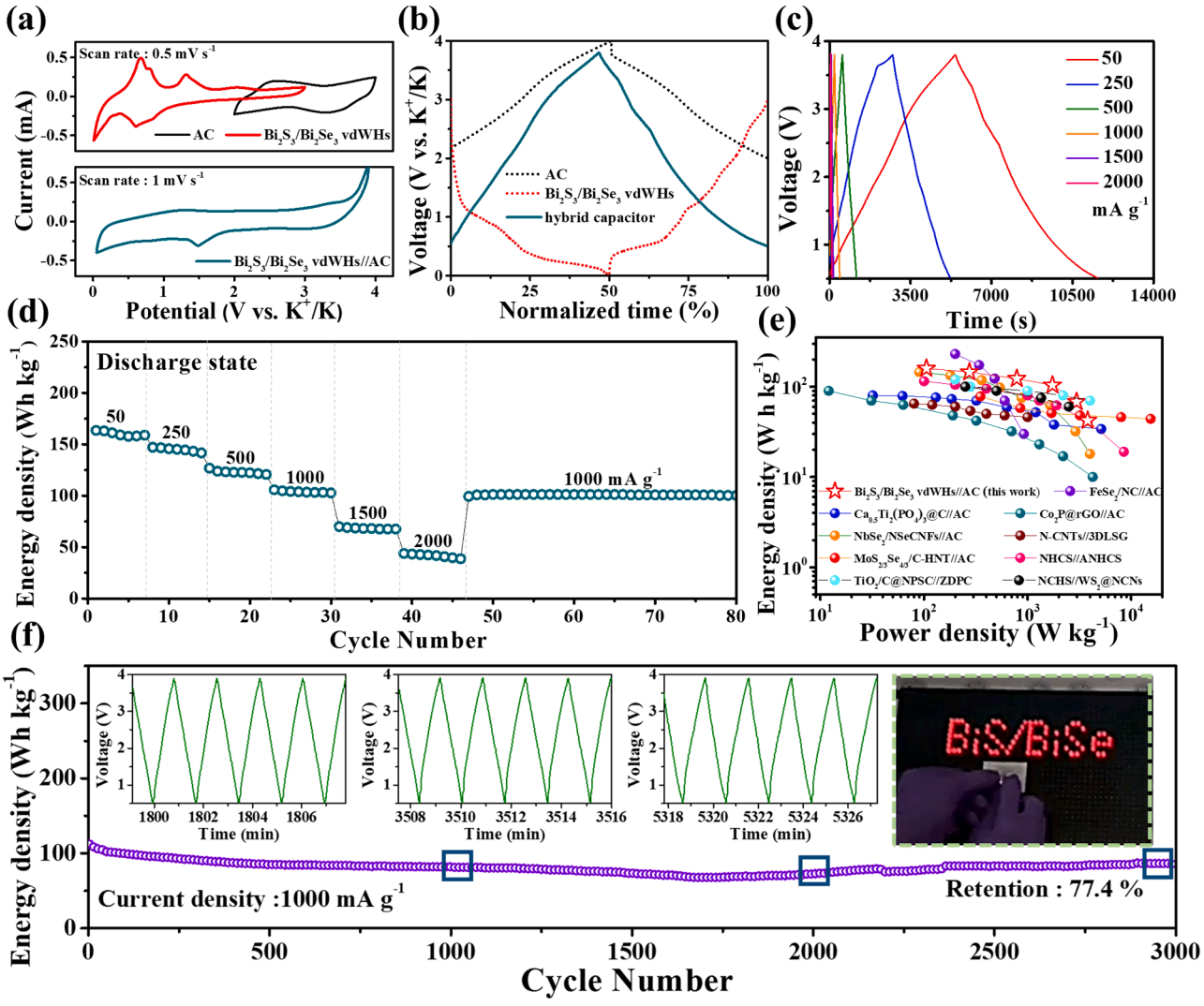

Fig. 9. Electrochemical characteristics of Bi_2S_3/Bi_2Se_3 vdWHs//AC PIHCs. (a) CV curves and (b) normalized GCD curves of a half cell and a full cell. (c, d) Rate performance at the current densities range from 50 to 3000 mA g^{-1}. (e) Ragone plot of the Bi_2S_3/Bi_2Se_3 vdWHs//AC PIHC full cell in comparison with the reported PIHCs. (g) The long-term cycling performance at 1000 mA g^{-1}: the retention capacity after for 3000 cycles is 77.4%. The insets present the voltage profiles and the demonstration digital picture in LED bulb lighting.

profiles exhibit a non-isosceles triangle curve according to the coupling of conversion-type anode and adsorption-type cathode. As shown in Fig. 9c, d, the Bi_2S_3/Bi_2Se_3 vdWHs//AC full capacitor achieves the energy densities of 158, 143, 122, 103, 68, and 43 Wh kg^{-1}at the current density of 50−2000 mA g^{-1}, respectively, based on the total active mass of Bi_2S_3/Bi_2Se_3 vdWHs and AC. When returned to 1000 mA g^{-1}, the energy density of PIHCs recovers to 101 mA h g^{-1}. In addition, the Ragone plot is a graph of specific energy versus specific power, with two logarithmic axes allowing the performance of different system to be compared. The electrochemical performance of Bi_2S_3/Bi_2Se_3 vdWHs//AC is comparable with other hybrid PIHCs, including $Ca_{0.5}Ti_2(PO_4)_3$@C //AC, [89], $NbSe_2$/NSeCNFs//AC, [90] $MoS_{2/3}Se_{4/3}$/C-HNT//AC, [91] TiO_2/C@NPSC//ZDPC, [92] $FeSe_2$/NC//AC, [93] Co_2P@rGO//AC, [94] N-CNTs//3D-LSG, [95] NHCS//ANHCS, [96] WS_2@NCNs //NCHS [97], as presented in Fig. 9e and Table S4. The cycling performance of PIHCs delivers attractive energy density of 106 Wh kg^{-1} at high current density of 1000 mA g^{-1}. After 3000 cycles, the retention of energy density is 77.4%, and the voltage profiles (insets of Fig. 10f) at 1000th, 2000th, and 3000th retain the similar shape without obvious overpotential during rapid ion-transfer process. Meanwhile, the Bi_2S_3/Bi_2Se_3 vdWHs//AC PIHC also lighted up 82 red LED bulbs as shown in the inset of Figs. 9f and S40. The outstanding performance of Bi_2S_3/Bi_2Se_3 vdWHs//AC full cells should be attributed to the advantages, including proper adsorption energy, sufficient diffusivity, and structural durability during fast ion transport.

3. Conclusions

For the first time, Bi_2S_3/Bi_2Se_3 vdWHs were fabricated with an efficient and rational design strategy *via* kinetics and mass transfer control with stabilizers and viscous solvents. The electrochemical kinetics and retention of the conversion reaction are significantly enhanced by the abundant network contacting the heterogeneous interface, as verified by both experiments and simulations. The lattice distortion and structural durability between Bi_2Se_3 and Bi_2S_3 are well preserved during charge-discharge procedure due to the ordered assembly of vdW heteroepitaxy. Therefore, the engineering of the heterojunction not only changes the trapping ability of the active intermediates and the electronic properties of the heterostructure, but also facilitates the diffusion of K ions with suitable adsorption energies. Due to the low diffusion barrier, K ions are easily adsorbed to the surface of the Bi_2S_3 nanowire network first, and then diffuse into the void space between each bundle of nanowires through the six pathways constructed by the regular growth of nanowires. Afterwards, K ions are shuttled into the heterointerface and Bi_2Se_3 nanoplates. Due to the topological effect on the surface of Bi_2Se_3, the smaller energy bandgap and electrical conductivity of Bi_2Se_3 can further facilitate the electron transfer in the interconnected structure, so that the charges are uniformly distributed around the whole heterostructure. The construction of the p-n heterojunction forms a built-in electric field between Bi_2S_3 and Bi_2Se_3, which provides an efficient shortcut for lateral and vertical charge transport. Even after the cycling process, the charge-transfer resistance and diffusion-controlled impedance of Bi_2S_3/Bi_2Se_3 vdWHs are much smaller than those of the hybrid Bi_2S_3 and Bi_2Se_3 materials without heterojunction (M-BSS). Electrons and K ions can still be easily transported through the inner and outer surfaces of the heterostructure, accompanied by reversible conversion reactions verified by operando and *ex situ* analyses. Notably, the PIB and PIHC full cells exhibit excellent cyclability and rate capability in the Ragone plots due to the high operating voltage window and capacity performance. Given the outstanding performance of regularly assembled vdWHs with network contact interfaces, our study can provide a reference and a reliable route to next-generation rechargeable energy storage through proof-of-concept experiments.

Data availability

The authors declare that the data supporting this study are available within the article. Furthermore, extra data are also available from the corresponding author upon request Eqs. (1), (2), (5).

CRediT authorship contribution statement

Yi-Yen Hsieh: Conceptualization, Methodology, Data curation. **Hsing-Yu Tuan:** Conceptualization, Resources, Supervision, Writing – review & editing.

Declaration of Competing Interest

The authors declare no competing financial interest.

Acknowledgments

This work was supported by the 2030 Cross-Generation Young Scholars Program by Ministry of Science and Technology, Taiwan (MOST 111-2628-E-007-008). H.-Y. Tuan also acknowledges the financial support of National Tsing Hua University, Taiwan, through the grant of 111QI030E1.

Supplementary materials

Supplementary material associated with this article can be found, in the online version, at doi:10.1016/j.ensm.2022.07.020.

References

[1] X. Min, J. Xiao, M. Fang, W.A. Wang, Y. Zhao, Y. Liu, A.M. Abdelkader, K. Xi, R. V. Kumar, Z. Huang, Potassium-ion batteries: outlook on present and future technologies, Energy Environ. Sci. 14 (2021) 2186–2243, https://doi.org/10.1039/D0EE02917C.
[2] S. Liu, L. Kang, J. Henzie, J. Zhang, J. Ha, M.A. Amin, M.S.A. Hossain, S.C. Jun, Y. Yamauchi, Recent advances and perspectives of battery-type anode materials for potassium ion storage, ACS Nano 15 (2021) 18931–18973, https://doi.org/10.1021/acsnano.1c08428.
[3] Y. An, Y. Tian, C. Wei, H. Jiang, B. Xi, S. Xiong, J. Feng, Y. Qian, Scalable and physical synthesis of 2D silicon from bulk layered alloy for lithium-ion batteries and lithium metal batteries, ACS Nano 13 (2019) 13690–13701, https://doi.org/10.1021/acsnano.9b06653.
[4] Y. An, Y. Tian, C. Wei, Y. Zhang, S. Xiong, J. Feng, Y. Qian, Recent advances and perspectives of 2D silicon: synthesis and application for energy storage and conversion, Energy Storage Mater. 32 (2020) 115–150, https://doi.org/10.1016/j.ensm.2020.07.006.
[5] K.T. Chen, S. Chong, L. Yuan, Y.C. Yang, H.Y. Tuan, Conversion-alloying dual mechanism anode: nitrogen-doped carbon-coated Bi_2Se_3 wrapped with graphene for superior potassium-ion storage, Energy Storage Mater. 39 (2021) 239–249, https://doi.org/10.1016/j.ensm.2021.04.019.
[6] C.B. Chang, K.T. Chen, H.Y. Tuan, Large-scale synthesis of few-layered copper antimony sulfide nanosheets as electrode materials for high-rate potassium-ion storage, J. Colloid Interface Sci. 608 (2022) 984–994, https://doi.org/10.1016/j.jcis.2021.09.154.
[7] S.B. Huang, Y.Y. Hsieh, K.T. Chen, H.Y. Tuan, Flexible nanostructured potassium-ion batteries, Chem. Eng. J. 416 (2021), 127697, https://doi.org/10.1016/j.cej.2020.127697.
[8] C.Y. Tsai, C.H. Chang, T.L. Kao, K.T. Chen, H.Y. Tuan, Shape matters: $SnP_{0.94}$ teardrop nanorods with boosted performance for potassium ion storage, Chem. Eng. J. 417 (2021), 128552, https://doi.org/10.1016/j.cej.2021.128552.
[9] J. Liao, C. Chen, Q. Hu, Y. Du, Y. He, Y. Xu, Z. Zhang, X. Zhou, A low-strain phosphate cathode for high-rate and ultralong cycle-life potassium-ion batteries, Angew. Chem. Int. Ed. 60 (2021) 25575–25582, https://doi.org/10.1002/anie.202112183.
[10] Y.Y. Hsieh, K.T. Chen, H.Y. Tuan, A synergetic SnSb-amorphous carbon composites prepared from polyesterification process as an ultrastable potassium-ion battery anode, Chem. Eng. J. 15 (2021), 130451, https://doi.org/10.1016/j.cej.2021.130451.
[11] K.T. Chen, H.Y. Tuan, Bi-Sb nanocrystals embedded in phosphorus as high-performance potassium ion battery electrodes, ACS Nano 14 (2020) 11648–11661, https://doi.org/10.1021/acsnano.0c04203.
[12] H. Liang, Y. Zhang, S. Hao, L. Cao, Y. Li, Q. Li, D. Chen, X. Wang, X. Guo, H. Li, Fast potassium storage in porous CoV_2O_6 nanosphere@ graphene oxide towards high-performance potassium-ion capacitors, Energy Storage Mater. 40 (2021) 250–258, https://doi.org/10.1016/j.ensm.2021.05.013.

[13] C.H. Chang, K.T. Chen, Y.Y. Hsieh, C.B. Chang, H.Y. Tuan, Crystal facet and architecture engineering of metal oxide nanonetwork anodes for high-performance potassium ion batteries and hybrid capacitors, ACS Nano 16 (2022) 1486–1501, https://doi.org/10.1021/acsnano.1c09863.
[14] W. Feng, H. Wang, Y. Jiang, H. Zhang, W. Luo, W. Chen, C. Shen, C. Wang, J. Wu, L. Mai, A strain-relaxation red phosphorus freestanding anode for non-aqueous potassium ion batteries, Adv. Energy Mater. (2022), 2103343, https://doi.org/10.1002/aenm.202103343.
[15] Y. Du, W. Weng, Z. Zhang, Y. He, J. Xu, J. Sun, J. Liao, J. Bao, X. Zhou, Candied-haws-like architecture consisting of FeS_2@ C core–shell particles for efficient potassium storage, ACS Mater. Lett. 3 (2021) 356–363, https://doi.org/10.1021/acsmaterialslett.1c00129.
[16] Y. He, Y. Xu, M. Zhang, J. Xu, B. Chen, Y. Zhang, J. Bao, X. Zhou, Confining ultrafine SnS nanoparticles in hollow multichannel carbon nanofibers for boosting potassium storage properties, Sci. Bull. 67 (2022) 151–160, https://doi.org/10.1016/j.scib.2021.09.020.
[17] Z. Li, R. Sun, Z. Qin, X. Liu, C. Wang, H. Fan, Y. Zhang, S. Lu, Recent progress of nanostructured metal chalcogenides and their carbon-based hybrids for advanced potassium battery anodes, Mater. Chem. Front. 5 (2021) 4401–4423, https://doi.org/10.1039/D1QM00085C.
[18] S. Shi, Z. Li, Y. Sun, B. Wang, Q. Liu, Y. Hou, S. Huang, J. Huang, Y. Zhao, A covalent heterostructure of monodisperse Ni_2P immobilized on N, P-co-doped carbon nanosheets for high performance sodium/lithium storage, Nano Energy 48 (2018) 510–517, https://doi.org/10.1016/j.nanoen.2018.04.001.
[19] G.J. Lai, L.M. Lyu, Y.S. Huang, G.C. Lee, M.P. Lu, T.P. Perng, M.Y. Lu, L.J. Chen, Few-layer WS_2–MoS_2 in-plane heterostructures for efficient photocatalytic hydrogen evolution, Nano Energy 81 (2021), 105608, https://doi.org/10.1016/j.nanoen.2020.105608.
[20] H. Shan, J. Qin, Y. Ding, H.M.K. Sari, X. Song, W. Liu, Y. Hao, J. Wang, C. Xie, J. Zhang, X. Li, Controllable heterojunctions with a semicoherent phase boundary boosting the potassium storage of $CoSe_2$/$FeSe_2$, Adv. Mater. 33 (2021), 2102471, https://doi.org/10.1002/adma.202102471.
[21] L. Cao, B. Luo, B. Xu, J. Zhang, C. Wang, Z. Xiao, S. Li, Y. Li, B. Zhang, G. Zou, H. Hou, X. Ou, X. Ji, Stabilizing intermediate phases via efficient entrapment effects of layered VS_4/SnS@ C heterostructure for ultralong lifespan potassium-ion batteries, Adv. Funct. Mater. 31 (2021), 2103802, https://doi.org/10.1002/adfm.202103802.
[22] C. Guo, W. Zhang, Y. Liu, J. He, S. Yang, M. Liu, Q. Wang, Z. Guo, Constructing CoO/Co_3S_4 heterostructures embedded in N-doped carbon frameworks for high-performance sodium-ion batteries, Adv. Funct. Mater. 29 (2019), 1901925, https://doi.org/10.1002/adfm.201901925.
[23] J. Wang, B. Wang, B. Lu, Nature of novel 2D van der Waals heterostructures for superior potassium ion batteries, Adv. Energy Mater. 10 (2020), 2000884, https://doi.org/10.1002/aenm.202000884.
[24] H. Li, C. Chen, Y. Yan, T. Yan, C. Cheng, D. Sun, L. Zhang, Utilizing the built-in electric field of P–N junctions to spatially propel the stepwise polysulfide conversion in lithium–sulfur batteries, Adv. Mater. 33 (2021), 2105067, https://doi.org/10.1002/adma.202105067.
[25] J. Zheng, Y. Wu, Y. Sun, J. Rong, H. Li, L. Niu, Advanced anode materials of potassium ion batteries: from zero dimension to three dimensions, Micro Nano Lett. 13 (2021) 1–37, https://doi.org/10.1007/s40820-020-00541-y.
[26] C. Gabbett, C.S. Boland, A. Harvey, V. Vega-Mayoral, R.J. Young, J.N. Coleman, The effect of network formation on the mechanical properties of 1D: 2D nano: nano composites, Chem. Mater. 30 (2018) 5245–5255, https://doi.org/10.1021/acs.chemmater.8b01945.
[27] Y. Zheng, T. Zhou, C. Zhang, J. Mao, H. Liu, Z. Guo, Boosted charge transfer in SnS/SnO_2 heterostructures: toward high rate capability for sodium-ion batteries, Angew. Chem. 128 (2016) 3469–3474, https://doi.org/10.1002/ange.201510978.
[28] M.I.B. Utama, Q. Zhang, J. Zhang, Y. Yuan, F.J. Belarre, J. Arbiol, Q. Xiong, Recent developments and future directions in the growth of nanostructures by van der Waals epitaxy, Nanoscale 5 (2013) 3570–3588, https://doi.org/10.1039/C3NR34011B.
[29] G. Jin, C.S. Lee, O.F. Okello, S.H. Lee, M.Y. Park, S. Cha, S.Y. Seo, G. Moon, S. Y. Min, D.H. Yang, Heteroepitaxial van der Waals semiconductor superlattices, Nat. Nanotechnol. 16 (2021) 1092–1098, https://doi.org/10.1038/s41565-021-00942-z.
[30] Y.J. Hong, C.H. Lee, Van der Waals heteroepitaxy of semiconductor nanowires. Semiconduct Semimet, Elsevier, 2015, pp. 125–172, https://doi.org/10.1016/bs.semsem.2015.07.002.
[31] J. Wang, J. Liu, H. Yang, D. Chao, J. Yan, S.V. Savilov, J. Lin, Z.X. Shen, MoS_2 nanosheets decorated Ni_3S_2@MoS_2 coaxial nanofibers: constructing an ideal heterostructure for enhanced Na-ion storage, Nano Energy 20 (2016) 1–10, https://doi.org/10.1016/j.nanoen.2015.12.010.
[32] P. Zhang, L. Yu, X.W. Lou, Construction of heterostructured Fe_2O_3-TiO_2 microdumbbells for photoelectrochemical water oxidation, Angew. Chem. Int. Ed. 57 (2018) 15076–15080, https://doi.org/10.1002/anie.201808104.
[33] Y. Wang, J. He, C. Liu, W.H. Chong, H. Chen, Thermodynamics versus kinetics in nanosynthesis, Angew. Chem. Int. Ed. 54 (2015) 2022–2051, https://doi.org/10.1002/anie.201402986.
[34] J. Wang, L. Li, H. Yu, F. Guan, D. Wang, Binary–Ternary Bi_2S_3–$AgBiS_2$ Rod-to-rod transformation via anisotropic partial cation exchange reaction, Inorg. Chem. 58 (2019) 12998–13006, https://doi.org/10.1021/acs.inorgchem.9b01917.
[35] X. Xu, C. Fan, Y. Wang, Z. Qi, B. Dai, H. Jiang, S. Wang, Q. Zhang, In-plane epitaxy of Bi2S3 nanowire arrays for ultrasensitive NIR photodetectors, Phys. Status Solidi (RRL)–Rap. Res. Lett. 14, 2000384 (2020). 10.1002/pssr.202000384.
[36] Y. Wang, J. Chen, P. Wang, L. Chen, Y.B. Chen, L.M. Wu, Syntheses, growth mechanism, and optical properties of [001]growing Bi_2S_3 nanorods, J. Phys. Chem. C 113 (2009) 16009–16014, https://doi.org/10.1021/jp904448k.
[37] A. Bera, S. Dey, A.J. Pal, Band mapping across a pn-junction in a nanorod by scanning tunneling microscopy, Nano Lett. 14 (2014) 2000–2005, https://doi.org/10.1021/nl500081m.
[38] C. Li, S. Dong, R. Tang, X. Ge, Z. Zhang, C. Wang, Y. Lu, L. Yin, Heteroatomic interface engineering in MOF-derived carbon heterostructures with built-in electric-field effects for high performance Al-ion batteries, Energy Environ. Sci. 11 (2018) 3201–3211, https://doi.org/10.1039/C8EE01046C.
[39] J. Wu, S. Liu, Y. Rehman, T. Huang, J. Zhao, Q. Gu, J. Mao, Z. Guo, Phase engineering of nickel sulfides to boost sodium-and potassium-ion storage performance, Adv. Funct. Mater. 31 (2021), 2010832, https://doi.org/10.1002/adfm.202010832.
[40] X. Wang, S. Zhang, Y. Shan, L. Chen, G. Gao, X. Zhu, B. Cao, X. He, *In situ* heterogeneous interface construction boosting fast ion/electron transfer for high-performances lithium/potassium storage, Energy Storage Mater. 37 (2021) 55–66, https://doi.org/10.1016/j.ensm.2021.01.027.
[41] T.T. Tran, J.R. Panella, J.R. Chamorro, J.R. Morey, T.M. McQueen, Designing indirect–direct bandgap transitions in double perovskites, Mater. Horiz. 4 (2017) 688–693, https://doi.org/10.1039/C7MH00239D.
[42] P. Makuła, M. Pacia, W. Macyk, How to Correctly Determine the Band gap Energy of Modified Semiconductor Photocatalysts based on UV–Vis Spectra, ACS Publications, 2018, pp. 6814–6817, https://doi.org/10.1021/acs.jpclett.8b02892.
[43] F. Ismail, Z. Hanafi, Some physico-chemical properties of bismuth chalcogenides X-Ray photoelectron and diffuse reflectance spectra, Z. Phys. Chem. 267 (1986) 667–672, https://doi.org/10.1515/zpch-1986-26782.
[44] A.R. Ettema, C. Haas, An X-ray photoemission spectroscopy study of interlayer charge transfer in some misfit layer compounds, J. Phys. Condens. Matter 5 (1993) 3817, https://doi.org/10.1088/0953-8984/5/23/008.
[45] J. Grigas, E. Talik, V. Lazauskas, X-ray photoelectron spectra and electronic structure of Bi_2S_3 crystals, Phys. Status Solidi 232 (2002) 220–230, https://doi.org/10.1002/1521-3951(200208)232:2<220::AID-PSSB220>3.0.CO;2-F.
[46] T. Takahashi, T. Sagawa, H. Hamanaka, Photoemission (XPS and UPS) study of amorphous Bi_2Se_3 film, J. Non-Cryst. Solids 65 (1984) 261–267, https://doi.org/10.1016/0022-3093(84)90051-6.
[47] K. Kim, S.Y. Lim, J. Kim, J.U. Lee, S. Lee, P. Kim, K. Park, S. Son, C.H. Park, J. G. Park, Antiferromagnetic ordering in van der Waals 2D magnetic material $MnPS_3$ probed by Raman spectroscopy, 2D Mater. 6 (2019), 041001, https://doi.org/10.1088/2053-1583/ab27d5.
[48] J. Zhong, J. Yu, L. Cao, C. Zeng, J. Ding, C. Cong, Z. Liu, Y. Liu, High-performance polarization-sensitive photodetector based on a few-layered $PdSe_2$ nanosheet, Nano Res. 13 (2020) 1780–1786, https://doi.org/10.1007/s12274-020-2804-y.
[49] H. Zhou, C.S. Simmons, M. Sarntinoranont, G. Subhash, Raman spectroscopy methods to characterize the mechanical response of soft biomaterials, Biomacromolecules 21 (2020) 3485–3497, https://doi.org/10.1021/acs.biomac.0c00818.
[50] T. Mohiuddin, A. Lombardo, R. Nair, A. Bonetti, G. Savini, R. Jalil, N. Bonini, D. Basko, C. Galiotis, N. Marzari, Uniaxial strain in graphene by Raman spectroscopy: G peak splitting, Grüneisen parameters, and sample orientation, Phys. Rev. B 79 (2009), 205433, https://doi.org/10.1103/PhysRevB.79.205433.
[51] J. Zhang, Z. Peng, A. Soni, Y. Zhao, Y. Xiong, B. Peng, J. Wang, M.S. Dresselhaus, Q. Xiong, Raman spectroscopy of few-quintuple layer topological insulator Bi2Se3 nanoplatelets, Nano Lett. 11 (2011) 2407–2414, https://doi.org/10.1021/nl200773n.
[52] Y. Li, L. Huang, B. Li, X. Wang, Z. Zhou, J. Li, Z. Wei, Co-nucleus 1D/2D heterostructures with Bi_2S_3 nanowire and MoS_2 monolayer: one-step growth and defect-induced formation mechanism, ACS Nano 10 (2016) 8938–8946, https://doi.org/10.1021/acsnano.6b04952.
[53] Y. Zhao, K.T.E. Chua, C.K. Gan, J. Zhang, B. Peng, Z. Peng, Q. Xiong, Phonons in Bi 2 S 3 nanostructures: Raman scattering and first-principles studies, Phys. Rev. B 84 (2011), 205330, https://doi.org/10.1103/PhysRevB.84.205330.
[54] D. Tuschel, Stress, strain, and Raman spectroscopy, Spectroscopy 34 (2019) 10–22, https://doi.org/10.1515/zkri-2018-2112.
[55] Q. Han, J. Chen, X. Yang, L. Lu, X. Wang, Preparation of uniform Bi2S3 nanorods using xanthate complexes of bismuth (III), J. Phys. Chem. C 111 (2007) 14072–14077, https://doi.org/10.1021/jp0742766.
[56] W. Yang, J. Yang, K. Zhao, Q. Gao, L. Liu, Z. Zhou, S. Hou, X. Wang, G. Shen, X. Pang, Low-noise dual-band polarimetric image sensor based on 1D Bi_2S_3 nanowire, Adv. Sci. 8 (2021), 2100075, https://doi.org/10.1002/advs.202100075.
[57] S. Xu, Y. Han, X. Chen, Z. Wu, L. Wang, T. Han, W. Ye, H. Lu, G. Long, Y. Wu, van der Waals epitaxial growth of atomically thin Bi_2Se_3 and thickness-dependent topological phase transition, Nano Lett. 15 (2015) 2645–2651, https://doi.org/10.1021/acs.nanolett.5b00247.
[58] M.-H. Doan, Y. Jin, S. Adhikari, S. Lee, J. Zhao, S.C. Lim, Y.H. Lee, Charge transport in MoS_2/WSe_2 van der Waals heterostructure with tunable inversion layer, ACS Nano 11 (2017) 3832–3840, https://doi.org/10.1021/acsnano.7b00021.
[59] M.B. Pinson, M.Z. Bazant, Theory of SEI formation in rechargeable batteries: capacity fade, accelerated aging and lifetime prediction, J. Electrochem. Soc. 160 (2012) A243, https://doi.org/10.1149/2.044302jes.
[60] B. Sun, Q. Zhang, C. Zhang, W. Xu, J. Wang, G. Yuan, W. Lv, X. Li, N. Yang, A passionfruit-like carbon-confined Cu_2ZnSnS_4 anode for ultralong-life sodium storage, Adv. Energy Mater. 11 (2021), 2100082, https://doi.org/10.1002/aenm.202100082.
[61] Y. Zhang, P. Chen, Q. Wang, Q. Wang, K. Zhu, K. Ye, G. Wang, D. Cao, J. Yan, Q. Zhang, High-capacity and kinetically accelerated lithium storage in MoO_3

enabled by oxygen vacancies and heterostructure, Adv. Energy Mater. 11 (2021), 2101712, https://doi.org/10.1002/aenm.202101712.
[62] S. Dong, D. Yu, J. Yang, L. Jiang, J. Wang, L. Cheng, Y. Zhou, H. Yue, H. Wang, L. Guo, Tellurium: a high-volumetric-capacity potassium-ion battery electrode material, Adv. Mater. 32 (2020), 1908027, https://doi.org/10.1002/adma.201908027.
[63] P. Liu, J. Han, K. Zhu, Z. Dong, L. Jiao, Heterostructure $SnSe_2$/ZnSe@ PDA nanobox for stable and highly efficient sodium-ion storage, Adv. Energy Mater. 10 (2020), 2000741, https://doi.org/10.1002/aenm.202000741.
[64] Q. Sun, D. Li, L. Dai, Z. Liang, L. Ci, Structural engineering of SnS_2 encapsulated in carbon nanoboxes for high-performance sodium/potassium-ion batteries anodes, Small 16 (2020), 2005023, https://doi.org/10.1002/smll.202005023.
[65] R. Xu, Y. Yao, H. Wang, Y. Yuan, J. Wang, H. Yang, Y. Jiang, P. Shi, X. Wu, Z. Peng, Unraveling the nature of excellent potassium storage in small-molecule Se@ Peapod-Like N-doped carbon nanofibers, Adv. Mater. 32 (2020), 2003879, https://doi.org/10.1002/adma.202003879.
[66] B. Sheng, L. Wang, H. Huang, H. Yang, R. Xu, X. Wu, Y. Yu, Boosting potassium storage by integration advantageous of defect engineering and spatial confinement: a case study of Sb_2Se_3, Small 16 (2020), 2005272, https://doi.org/10.1002/smll.202005272.
[67] X. Ren, D. Yu, L. Yuan, Y. Bai, K. Huang, J. Liu, S. Feng, *In situ* exsolution of Ag from $AgBiS_2$ nanocrystal anode boosting high-performance potassium-ion batteries, J. Mater. Chem. A 8 (2020) 15058–15065, https://doi.org/10.1039/D0TA03964K.
[68] L. Fan, S. Chen, R. Ma, J. Wang, L. Wang, Q. Zhang, E. Zhang, Z. Liu, B. Lu, Ultrastable potassium storage performance realized by highly effective solid electrolyte interphase layer, Small 14 (2018), 1801806, https://doi.org/10.1002/smll.201801806.
[69] A.F. Pedersen, M. Escudero-Escribano, B. Sebok, A. Bodin, E. Paoli, R. Frydendal, D. Friebel, I.E. Stephens, J. Rossmeisl, I. Chorkendorff, Operando XAS study of the surface oxidation state on a monolayer IrO x on RuO x and Ru oxide based nanoparticles for oxygen evolution in acidic media, J. Phys. Chem. B 122 (2018) 878–887, https://doi.org/10.1021/acs.jpcb.7b06982.
[70] L.A. Walsh, C.L. Hinkle, van der Waals epitaxy: 2D materials and topological insulators, Appl. Mater. Today 9 (2017) 504–515, https://doi.org/10.1016/j.apmt.2017.09.010.
[71] A. Koma, Van der Waals epitaxy—a new epitaxial growth method for a highly lattice-mismatched system, Thin Solid Films 216 (1992) 72–76, https://doi.org/10.1016/0040-6090(92)90872-9.
[72] C. Zhang, A. Wang, J. Zhang, X. Guan, W. Tang, J. Luo, 2D materials for lithium/sodium metal anodes, Adv. Energy Mater. 8 (2018), 1802833, https://doi.org/10.1002/aenm.201802833.
[73] Z. Li, K. Zhu, P. Liu, L. Jiao, 3D confinement strategy for dendrite-free sodium metal batteries, Adv. Energy Mater. 12 (2022), 2100359, https://doi.org/10.1002/aenm.202100359.
[74] H. Wang, D. Yu, C. Kuang, L. Cheng, W. Li, X. Feng, Z. Zhang, X. Zhang, Y. Zhang, Alkali metal anodes for rechargeable batteries, Chem 5 (2019) 313–338, https://doi.org/10.1016/j.chempr.2018.11.005.
[75] A. Zhou, W. Cheng, W. Wang, Q. Zhao, J. Xie, W. Zhang, H. Gao, L. Xue, J. Li, Hexacyanoferrate-type Prussian blue analogs: principles and advances toward high-performance sodium and potassium ion batteries, Adv. Energy Mater. 11 (2021), 2000943, https://doi.org/10.1002/aenm.202000943.
[76] J. Liao, Q. Hu, Y. Yu, H. Wang, Z. Tang, Z. Wen, C. Chen, A potassium-rich iron hexacyanoferrate/dipotassium terephthalate@ carbon nanotube composite used for K-ion full-cells with an optimized electrolyte, J. Mater. Chem. A 5 (2017) 19017, https://doi.org/10.1039/C7TA05460B. -19024.
[77] L. Xue, Y. Li, H. Gao, W. Zhou, X. Lü, W. Kaveevivitchai, A. Manthiram, J. B. Goodenough, Low-cost high-energy potassium cathode, J. Am. Chem. Soc. 139 (2017) 2164–2167, https://doi.org/10.1021/jacs.6b12598.
[78] Y. Sun, C. Liu, J. Xie, D. Zhuang, W. Zheng, X. Zhao, Potassium manganese hexacyanoferrate/graphene as a high-performance cathode for potassium-ion batteries, New J. Chem. 43 (2019) 11618–11625, https://doi.org/10.1039/C9NJ02085C.
[79] Y. Hu, W. Tang, Q. Yu, X. Wang, W. Liu, J. Hu, C. Fan, Novel insoluble organic cathodes for advanced organic K-ion batteries, Adv. Funct. Mater. 30 (2020), 2000675, https://doi.org/10.1002/adfm.202000675.
[80] R.A. Adams, A. Varma, V.G. Pol, Temperature dependent electrochemical performance of graphite anodes for K-ion and Li-ion batteries, J. Power Sources 410 (2019) 124–131, https://doi.org/10.1016/j.jpowsour.2018.11.007.
[81] X.D. He, Z.H. Liu, J.Y. Liao, X. Ding, Q. Hu, L.N. Xiao, S. Wang, C.H. Chen, A three-dimensional macroporous antimony@ carbon composite as a high-performance anode material for potassium-ion batteries, J. Mater. Chem. A 7 (2019) 9629–9637, https://doi.org/10.1039/C9TA01968E.
[82] W. Qiu, H. Xiao, Y. Li, X. Lu, Y. Tong, Nitrogen and phosphorus codoped vertical graphene/carbon cloth as a binder-free anode for flexible advanced potassium ion full batteries, Small 15 (2019), 1901285, https://doi.org/10.1002/smll.201901285.
[83] R. Verma, P.N. Didwal, H.S. Ki, G. Cao, C.J. Park, SnP_3/carbon nanocomposite as an anode material for potassium-ion batteries, ACS Appl. Mater. Interfaces 11 (2019) 26976–26984, https://doi.org/10.1021/acsami.9b08088.
[84] K. Wu, X. Cao, M. Li, B. Lei, J. Zhan, M. Wu, Bottom-up synthesis of MoS_2/CNTs hollow polyhedron with 1T/2H hybrid phase for superior potassium-ion storage, Small 16 (2020), 2004178, https://doi.org/10.1002/smll.202004178.
[85] P. Xiong, J. Wu, M. Zhou, Y. Xu, Bismuth–antimony alloy nanoparticle@ porous carbon nanosheet composite anode for high-performance potassium-ion batteries, ACS Nano 14 (2019) 1018–1026, https://doi.org/10.1021/acsnano.9b08526.
[86] Y. Xu, C. Zhang, M. Zhou, Q. Fu, C. Zhao, M. Wu, Y. Lei, Highly nitrogen doped carbon nanofibers with superior rate capability and cyclability for potassium ion batteries, Nat. Commun. 9 (2018) 1–11, https://doi.org/10.1038/s41467-018-04190-z.
[87] H. Liu, H. Du, W. Zhao, X. Qiang, B. Zheng, Y. Li, B. Cao, Fast potassium migration in mesoporous carbon with ultrathin framework boosting superior rate performance for high-power potassium storage, Energy Storage Mater. 40 (2021) 490–498.
[88] Y. Wu, Y. Sun, Y. Tong, X. Liu, J. Zheng, D. Han, H. Li, L. Niu, Recent advances in potassium-ion hybrid capacitors: electrode materials, storage mechanisms and performance evaluation, Energy Storage. Mater. 41 (2021) 108–132, https://doi.org/10.1016/j.ensm.2021.05.045.
[89] Z. Zhang, M. Li, Y. Gao, Z. Wei, M. Zhang, C. Wang, Y. Zeng, B. Zou, G. Chen, F. Du, Fast potassium storage in hierarchical $Ca_{0.5}Ti_2(PO_4)_3$@ C microspheres enabling high-performance potassium-ion capacitors, Adv. Funct. Mater. 28 (2018), 1802684, https://doi.org/10.1002/adfm.201802684.
[90] M. Chen, L. Wang, X. Sheng, T. Wang, J. Zhou, S. Li, X. Shen, M. Zhang, Q. Zhang, X. Yu, An ultrastable nonaqueous potassium-ion hybrid capacitor, Adv. Funct. Mater. 30 (2020), 2004247, https://doi.org/10.1002/adfm.202004247.
[91] J. Gao, G. Wang, Y. Liu, J. Li, B. Peng, S. Jiao, S. Zeng, G. Zhang, Ternary molybdenum sulfoselenide based hybrid nanotubes boost potassium-ion diffusion kinetics for high energy/power hybrid capacitors, J. Mater. Chem. A 8 (2020) 13946–13954, https://doi.org/10.1039/D0TA01786H.
[92] H. Li, J. Chen, L. Zhang, K. Wang, X. Zhang, B. Yang, L. Liu, W. Liu, X. Yan, A metal–organic framework-derived pseudocapacitive titanium oxide/carbon core/shell heterostructure for high performance potassium ion hybrid capacitors, J. Mater. Chem. A 8 (2020) 16302–16311, https://doi.org/10.1039/D0TA04912C.
[93] J. Ge, B. Wang, J. Wang, Q. Zhang, B. Lu, Nature of FeSe2/N-C anode for high performance potassium ion hybrid capacitor, Adv. Energy Mater. 10 (2020), 1903277, https://doi.org/10.1002/aenm.201903277.
[94] Y. Wang, Z. Zhang, G. Wang, X. Yang, Y. Sui, F. Du, B. Zou, Ultrafine Co_2 P nanorods wrapped by graphene enable a long cycle life performance for a hybrid potassium-ion capacitor, Nanoscale Horiz. 4 (2019) 1394–1401, https://doi.org/10.1039/C9NH00211A.
[95] M. Moussa, S.A. Al-Bataineh, D. Losic, D.P. Dubal, Engineering of high-performance potassium-ion capacitors using polyaniline-derived N-doped carbon nanotubes anode and laser scribed graphene oxide cathode, Appl. Mater. Today 16 (2019) 425–434, https://doi.org/10.1016/j.apmt.2019.07.003.
[96] D. Qiu, J. Guan, M. Li, C. Kang, J. Wei, Y. Li, Z. Xie, F. Wang, R. Yang, Kinetics enhanced nitrogen-doped hierarchical porous hollow carbon spheres boosting advanced potassium-ion hybrid capacitors, Adv. Funct. Mater. 29 (2019), 1903496, https://doi.org/10.1002/adfm.201903496.
[97] Y. Li, Y. Yang, P. Zhou, T. Gao, Z. Xu, S. Lin, H. Chen, J. Zhou, S. Guo, Enhanced cathode and anode compatibility for boosting both energy and power densities of Na/K-ion hybrid capacitors, Matter 1 (2019) 893–910, https://doi.org/10.1016/j.matt.2019.04.003.